













Cite this: DOI: 10.1039/d5nr00863h

# Tunable and robust optical and structural properties of a cooperative squaraine-dye aggregate-DNA DX-DAE tile system†

Simon K. Roy, <sup>a</sup> Nolan Olasso, <sup>b</sup> Paul H. Davis, <sup>a</sup> Olga A. Mass, <sup>a</sup> Keitel Cervantes-Salguero, <sup>a</sup> Jeunghoon Lee, <sup>a,c</sup> Ryan D. Pensack, <sup>a</sup> John A. Hall, <sup>a,d</sup> Bernard Yurke <sup>\*a,b</sup> and William B. Knowlton <sup>\*a,b</sup>

Molecular excitons, which are excitations delocalized over multiple dyes in a wavelike manner, are of interest for a wide range of applications, including quantum information science. Numerous studies have templated a variety of synthetic dyes via a DNA scaffold to induce dye aggregation to create molecular excitons upon photoexcitation. Dye aggregate optical properties are critically dependent on relative dye geometry and local environment; therefore, an understanding of dye–dye and DNA–dye interactions is critical for advancing toward more complex DNA–dye systems. The extensively studied DNA Holliday junction (HJ) and less-studied double-crossover (DX) tile motif are fundamental test beds for designing complex and ultimately modular DNA–dye architectures. Here, we report the first study of single-linked squaraine dye aggregation and exciton delocalization on a larger and more stable (compared with the HJ) DX tile motif. We first highlight a few DNA–dye constructs that support single dyes and aggregates with distinct optical properties that are both tunable—through sample design, buffer conditions, and heat treatment—and robust to environment changes, including transfer to solid phase. Next, we assess several experimental and design considerations that demonstrate directed dye-driven assembly of a novel double-tile DNA configuration. Our results demonstrate that single-linked squaraine dyes templated to DX tiles provide a viable research path to design and evaluate dye aggregate networks that support exciton delocalization. We include herein the first report of exciton delocalization in the solid phase in a DNA–dye construct. Additionally, our findings indicate that dye aggregation impacts the assembly of the DNA–dye construct, and, in some cases, thereby cooperates with the DNA to determine a final robust system configuration. Finally, we show that a controlled annealing schedule can be employed to promote the homogeneous assembly of DNA–dye constructs. The findings in this study contribute to the understanding of DNA–dye systems and the relevant factors involved in their directed assembly to achieve specific constructs with desirable properties.

Received 26th February 2025,  
Accepted 1st May 2025  
DOI: 10.1039/d5nr00863h  
rsc.li/nanoscale

## 1. Introduction

Molecular excitons arising from the collective photoexcitation of conjugated organic molecules (*i.e.*, dyes) have been extensively studied for their unique properties and varied potential

applications.<sup>1–3</sup> A hallmark property of molecular excitons is the dipole–dipole induced delocalization of the excitation across participating dyes. A variety of dyes with distinct properties and of either natural or synthetic origin can be considered. Beginning with the initial observations of spontaneously aggregated dyes in solution<sup>4,5</sup> and the foundational molecular exciton theory put forth by Kasha and coworkers,<sup>6,7</sup> it is clear that the properties of interacting dyes are critically dependent on dye identity, number, and geometry of their interactions. Nature demonstrates the potential for efficient energy transport using dye-generated molecular excitons in photosynthetic systems;<sup>8–11</sup> however, the fine control of dye arrays afforded by proteins in natural systems is beyond the current state of research capabilities due to the complexity of protein folding. Instead, deoxyribonucleic acid (DNA) has been established as a viable platform for developing self-assembled

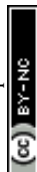
<sup>a</sup>Micron School of Materials Science & Engineering, Boise State University, Boise, Idaho 83725, USA. E-mail: BernardYurke@boisestate.edu, bknowlton@boisestate.edu

<sup>b</sup>Department of Electrical & Computer Engineering, Boise State University, Boise, Idaho 83725, USA

<sup>c</sup>Department of Chemistry and Biochemistry, Boise State University, Boise, Idaho 83725, USA

<sup>d</sup>Division of Research and Economic Development, Boise State University, Boise, Idaho 83725, USA

† Electronic supplementary information (ESI) available. See DOI: <https://doi.org/10.1039/d5nr00863h>



nanoscale systems<sup>2</sup> due to its well-understood design rules, commercial availability, and variety of methods for functionalizing a given strand or array with dye molecules.

DNA nanotechnology offers a vast and well-explored design space with the ability to self-assemble complex structures at the nanoscale.<sup>12–16</sup> In particular, DNA has shown specific potential for directed assembly of functional networks of dyes with applications in multiple fields, including light-harvesting,<sup>17</sup> nanophotonics,<sup>2</sup> bio-imaging, and other applications.<sup>18</sup> Recently, several authors have contributed further to the theoretical and application frameworks by suggesting electromagnetically coupled dye molecules may have potential applications in quantum information science (QIS).<sup>19–22</sup> For example, complete sets of dye-based quantum gates have been recently described that would enable universal quantum computation;<sup>20,22</sup> however, to realize such devices requires precise spatial control of dyes and aggregates and their self-assembly behavior, especially as related to multi-helical DNA templates such as double-crossover (DX) tiles and DNA origami constructs. Developing a detailed understanding of the basic components of such systems (*i.e.*, DNA template, dyes, and their surrounding condensed phase environments), how they interact with each other, and ultimately their resultant system properties is essential for identifying and implementing design rules that achieve desired dye–dye interactions in concert with predictable assembly of the DNA architecture.<sup>3,23</sup> The ability to predict and control such complex interactions can lead to potential benefits across various applications but realization requires further advances in our understanding of integrated DNA–dye systems.

### 1.1. Advances in DNA architecture and DNA–dye constructs

Seminal works by Seeman and coworkers<sup>24–27</sup> developed the basic building blocks of branched-junction DNA nanostructures, such as the immobile Holliday junction (HJ) tile and DX-tile motifs, that serve as the basis for programmed assembly of more complex nanostructures. Subsequently, many examples now exist of assembling distinct DX tiles into 1D,<sup>28</sup> 2D,<sup>29–31</sup> and 3D<sup>32</sup> arrays using short, programmed “sticky ends” on each tile to enable selective hybridization with other pre-assembled tiles. This bottom-up approach facilitates the development of distinct tile structures that can be combined to assemble specific networks of tiles. Each modular construct can then be functionalized with a unique custom array of dyes, thus providing a path forward to design more advanced assemblies or networks of dyes. Therefore, the fundamental HJ and DX tiles serve as useful and efficient test beds to explore the design space for arranging dyes and dye-aggregates using DNA.

The immobile HJ is now a rather well-studied template for directing dye aggregation due to its relatively simple architecture (one branch point), few components (four distinct DNA strands), and ease with which multiple dyes can be brought into close proximity to enable dipole–dipole coupling. Recently, the HJ has been utilized as a structural platform to create and characterize aggregates using a variety of dyes and

dye-attachment methods. For example, double-linked cyanine dyes have been incorporated into the DNA backbone *via* covalent bonding to form predominantly co-facially stacked (so-called H) aggregates.<sup>33–37</sup> Variants of squaraine and other dyes also have been shown to form aggregates with a variety of geometries with distinct optical properties when attached to HJ strands by a single, long (~2 nm) flexible linker covalently bonded to a modified nucleobase.<sup>38–44</sup> Although the HJ is useful for inducing dye aggregation, the geometric flexibility of the single branch point can be problematic for forming homogeneous structures due to a tendency of the HJ to take on different conformations (so-called open and two stacked isomers) depending on the nucleotides at the branch point and solution conditions of the study sample.

The DX tile represents the next step in complexity of DNA templates. The DX tile motif extends the HJ motif by incorporating an additional crossover junction that imparts rigidity to the system by coupling the bending and twisting modes of the DNA to increase persistence length.<sup>45</sup> This configuration possibly mitigates DNA breathing<sup>46</sup> effects, while also reducing the structural heterogeneity arising from conformational changes occurring in the HJ (see Cervantes-Salguero *et al.* for examples in which a HJ's conformation is restricted *via* origami<sup>47</sup>). The additional crossover also acts to keep the two linked helices in a roughly planar configuration. One of the fundamental DX tile designs is the DAE (Double crossover; Anti-parallel helices; Even number of half-turns of a helix between crossovers).<sup>25,26</sup> Although recent advances have been made in refining DX tiles with parallel helices,<sup>48</sup> designs with anti-parallel helices tend to be more broadly studied. Studies of excitonic behavior in DX-tile-dye systems has been more limited than studies using the HJ motif. The DX tile<sup>49–51</sup> and larger DNA networks<sup>17</sup> have been used as templates to produce cyanine-derivative aggregates *via* non-covalent DNA groove binding. Those configurations result in head-to-tail stacked (or J) aggregates whose geometry facilitates Förster resonance energy transfer (FRET) through one or more aggregates arranged between donor and acceptor pairs. The DX tile motif also has been used to template double (covalently) tethered Cy3 cyanine dyes and aggregates resulting in exciton delocalization and FRET;<sup>52,53</sup> however, the preceding studies are the extent of studying excitonic coupling in DX tile-templated dye aggregates. Therefore, and importantly, research has yet to address, among other considerations, single-linker dyes in higher order DNA templates.

### 1.2. Key knowledge gaps

Critical to understanding DNA–dye aggregate assembly rules and aggregation behavior is understanding how dye identity, additional dye functionalization, and DNA attachment method, including linker number, length, hydrophobicity, and chemistry of attachment, will influence its interactions with the DNA template and final system properties. Therefore, equally as important in understanding the behavior of DNA–dye systems generally is the development of a diverse toolbox of dyes and their linking methods that, in combination with a more complete understanding of how these affect their inter-



actions with different DNA templates, will provide insight into the potential strengths and weaknesses of each approach. As alluded to by Hart *et al.*,<sup>3</sup> future excitonic systems will likely require combining various approaches to optimize the properties of individual components; thus, it is beneficial for the field to develop design rules to promote desirable excitonic properties for a variety of dyes and DNA templates. Besides those studies previously cited, relevant past work includes synthesis and characterization of many DNA-dye systems that show signatures of exciton delocalization, including (but not limited to) intercalating dyes such as thiazole orange,<sup>54</sup> photo-synthetic bacteriochlorin analogs,<sup>55</sup> groove-assembled cyanine dyes,<sup>17,51</sup> and covalently attached perylene,<sup>56</sup> cyanine,<sup>34,35,52,57–59</sup> and squaraine dyes.<sup>38–42,60</sup>

Squaraine dyes—like cyanines—have been a focus of recent studies owing to their large transition-dipole moments (TDM) and options for functionalization to modify and study changes in dye-aggregate properties due to sterics, charge asymmetry, and hydrophobicity. Squaraines have been used for exploring exciton delocalization using multiple linking methods, including directly linking two squaraines covalently,<sup>61</sup> linking individual squaraines to DNA with two covalent linkers,<sup>62</sup> and exploring single-linker squaraines linked to DNA with differing lengths of carbon-based linkers.<sup>43,63</sup> The choice of linking scheme may be critical to the final system behavior. For example, and relevant to this study, potential challenges are associated with using dyes attached by single linkers.<sup>62</sup> Single-linker dyes have more freedom to sample the potential configuration space *versus* double-linker dyes, which may allow their active participation in determining aggregate geometry. This potential behavior enables the study of a truly cooperative DNA-dye system in which, though not necessarily to the same degree, the dyes also determine the final configuration and properties of the integrated system. As a result, for this study, a single-linker, symmetric, and hydrophobic di-chloro squaraine (SQ-Cl<sub>2</sub>) was selected for its strong coupling characteristics—when previously templated by a DNA HJ—and minimal sterics that further promote close-packed dye aggregates<sup>42,64</sup> with the goal of studying monomer and aggregate properties when templated to a DX-DAE tile.

Moreover, most existing studies have not focused on how changes in sample preparation conditions and eventual conditions of the bath (local environment) may affect DNA-dye assembly and ultimate behavior. In addition, with a limited exception,<sup>65</sup> studies to date have focused on DNA-dye system behavior in the liquid phase and do not report what occurs when the constructs are in the solid phase (*i.e.*, dried). Directed assembly of modular pre-assembled components—such as arrays of dyes templated on DX tiles—into complex and functional systems may require production of such components in their optimal environment and subsequent transfer to differing conditions for further assembly and processing. It is highly likely that integration of DNA-dye systems in electronic-based applications (*e.g.*, QIS, nanophotonics, *etc.*) will require that dye-aggregate behavior be maintained in the solid phase when immobilized on a surface or completely removed

from their native solvent. Although dehydration of DNA is expected to shift its conformation from the B-form to the A-form of the double helix, the DNA is generally expected to remain hybridized. Thus, it is of interest to demonstrate how different factors, such as salt and sample concentrations, dye placement conditions, and annealing protocols affect final system properties and whether desirable system properties achieved in solution (*i.e.*, exciton delocalization) can be maintained when the construct is dried on a surface.

### 1.3. Research objectives

To address the above knowledge gaps, we investigate the following four research objectives. First, we show that hydrophobic squaraine dyes with extended, single linkers can be templated to DX tiles to form a prototypical, integrated DNA-dye system that is cooperative in nature. Current literature suggests either (1) dyes with long, flexible single linkers can create DNA-dye construct control challenges<sup>62</sup> or (2) aggregate construct control for any dye type can best be achieved by manipulating and constraining DNA configurations and conformations without explicitly considering the dye's impact on the DNA itself. Here, we show the benefits of a DNA-dye system in which single-linker dyes significantly influence the final configurations of the DNA template and associated aggregate construct properties. As a prototype system, we contend that our system has the potential for transferring/scaling its system behavioral attributes to other similar dyes and to larger DNA modular assemblies and networks.

Second, in particular, we show that our DNA-dye system can form single dye and dye-aggregate constructs with tunable (*i.e.*, final construct configurations and spectra), reproducible, and desirable properties, including strongly coupled dye aggregates that exhibit robust and homogeneous absorption spectra. By robust, we mean that once the aggregate is formed, its spectral characteristics are insensitive to subsequent environmental changes and also are maintained over time. Third, we elucidate the roles of specific factors, including dye-dye interactions, dye location on the tile, sample concentration, solvent properties, and annealing details, and their influence on DNA-dye system behavior and resultant final configurations, their associated impact on single dye and dye aggregate properties, and the extent to which these factors can be controlled and adjusted to drive different outcomes. Finally, we demonstrate that desirable single dye and dye aggregate properties created in the liquid phase show the same behavior in solid phase, including a first report of exciton delocalization in solid-phase DNA-dye aggregate systems.

## 2. Materials and methods

### 2.1. Dye materials

Indolenine squaraine dyes functionalized with chlorine atoms (SQ-Cl<sub>2</sub>; Fig. 1a) were procured from SETA BioMedicals (Urbana-Champaign, Illinois). The synthesis of SQ-Cl<sub>2</sub> has been previously reported.<sup>42</sup>



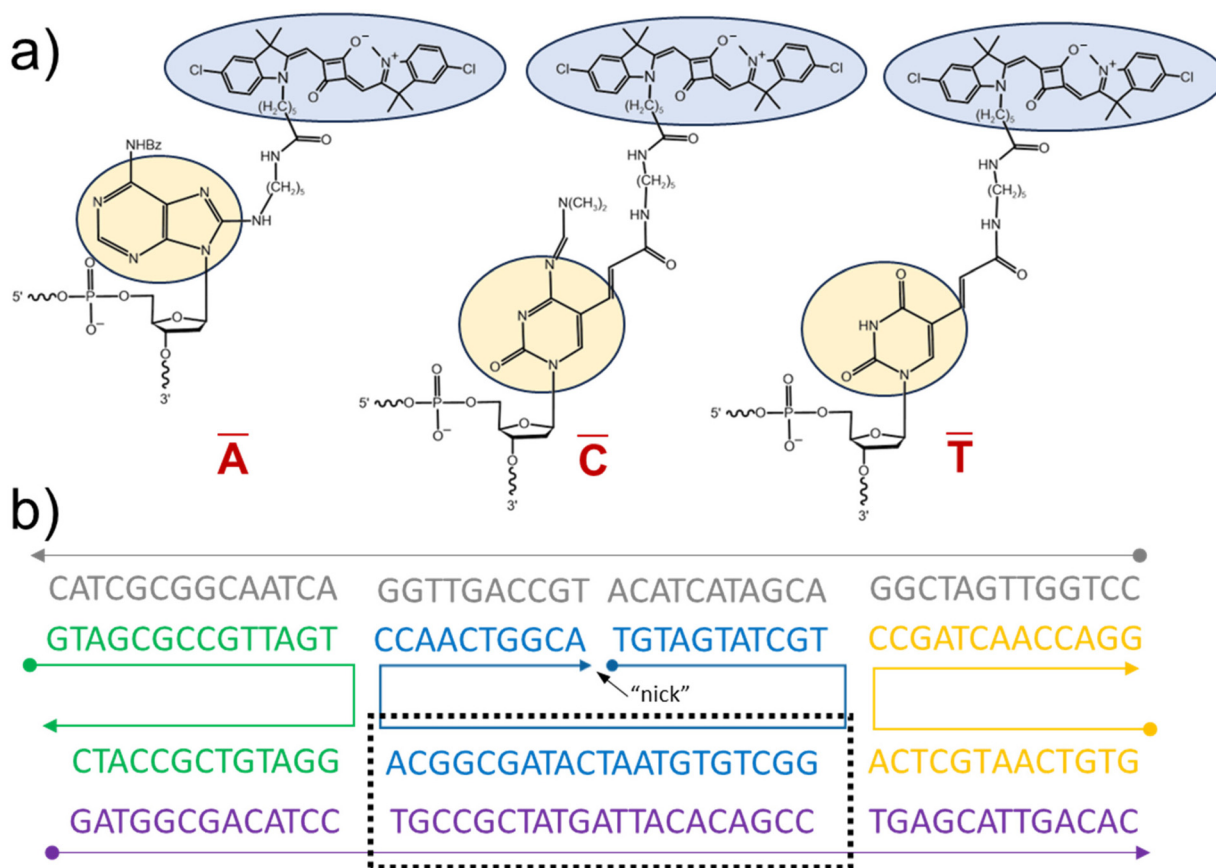


**Fig. 1** (a) Chemical structures of SQ-Cl<sub>2</sub> (blue ovals) and linker-modified nucleobases (yellow ovals). The linker-modified bases are denoted by the symbols:  $\bar{A}$  = modified adenine,  $\bar{C}$  = modified cytosine, and  $\bar{T}$  = modified thymine. These symbols are used in later figures to indicate dye attachments. Modified bases, sourced from Glenn Research were functionalized by IDT with SQ-Cl<sub>2</sub>, which was obtained from SETA BioMedicals as an NHS-ester derivative. (b) Nucleobase sequences for the DX-DAE tile. Continuous strands are color coordinated with circles and arrows representing the 5' and 3' ends, respectively. All dyes were covalently linked to the continuous DNA duplex spanning the two crossovers outlined in black dots. The blue-colored strand spanning both helical domains on the interior of the DX tile will be subsequently referred to as the central circular strand, whereas its complement in the region containing dyes will be referred to as the linear strand. Unless otherwise noted, only this portion of the sequences will be reproduced in later figures. See ESI section S1† for full sequences for all samples.

## 2.2. DNA construct synthesis

DNA sequences were synthesized, functionalized with squaraine dyes, and lyophilized by Integrated DNA Technology, Inc. (IDT, Coralville, Iowa). Non-functionalized DNA strands were purified by standard desalting. Dye-labeled strands were purified by dual high-performance liquid chromatography (HPLC) and dyes were attached by IDT to modified adenine, thymine, and cytosine nucleosidic linkers, C6 dA, C6 dT, and C6 dC, respectively (Fig. 1a).

All DNA strands were rehydrated with Type 1 ultrapure water (Barnstead Nanopure, Thermo Scientific) to a stock concentration of  $\sim 50 \mu\text{M}$ . Stock concentrations were verified with a Nanodrop One (Thermo Scientific) using manufacturer-provided DNA extinction data. DNA was combined in equimolar quantities to produce each construct. DX-DAE tile sequences were modified by IDT from previously published DX tile designs<sup>25</sup> by removing unpaired bases ("sticky ends") from the terminal ends of the tile and replacing those bases selected as dye attachment points with their linker-modified substitute.

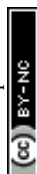
Unless otherwise noted, all DNA constructs were prepared in  $1\times$  tris-borate-EDTA (TBE), 15 mM MgCl<sub>2</sub>, and all samples were prepared to a nominal  $1 \mu\text{M}$  concentration and annealed (Mastecycler Nexus, Eppendorf) at  $95^\circ$  for 5 minutes, then slowly cooled to room temperature ( $\sim 22^\circ\text{C}$ ) at a rate of  $\sim -0.4^\circ\text{C min}^{-1}$ .

## 2.3. Absorption spectroscopy

Steady-state, ensemble absorption data were collected using a Cary-5000 ultraviolet-visible (UV-Vis) spectrometer (Agilent; wavelength accuracy:  $\pm 0.08 \text{ nm}$ ). Sample absorption was collected at  $22^\circ\text{C}$  (Peltier temperature controlled) using a 1 cm pathlength quartz cuvette (50  $\mu\text{L}$ ; Starna). Absorption was monitored from 230 nm to 800 nm in 1 nm steps with a 2 nm spectral bandwidth.

## 2.4. Circular dichroism

Circular dichroism (CD) spectra were collected using a JASCO J-1500 CD spectrophotometer (JASCO; wavelength accuracy:



$\pm 0.1$  nm [163 to 250 nm],  $\pm 0.2$  nm [250 to 500 nm],  $\pm 0.5$  nm [500 to 800 nm]). All CD data were collected from the same solution as the corresponding steady-state absorption data. Unless noted, all data were collected at 22 °C (Peltier temperature controlled) using a 1 cm pathlength quartz cuvette (100  $\mu$ L; JASCO) in 1 $\times$  TBE, 15 mM MgCl<sub>2</sub>, with a scan rate of 500 nm min<sup>-1</sup> scan rate. Reported spectra are the average of three accumulations per sample.

## 2.5. Steady-state fluorescence

Samples for all fluorescence-based techniques were prepared such that the absorbance (optical density) at the excitation wavelength was  $\sim 0.1$  or less in a 1 cm pathlength to ensure uniform illumination of the sample throughout the beam path. Steady-state fluorescence data were collected using a Fluorolog 3 spectrophotometer (Horiba; wavelength accuracy:  $\pm 0.3$  nm) using a 1 cm pathlength quartz cuvette (50  $\mu$ L; Starna) at 22 °C. Additional absorption data were collected to process the fluorescence data (ESI section S4†). Data were processed initially by subtracting a buffer signal. These data were corrected first for instrument efficiency using a manufacturer-provided correction curve and then by dividing by the absorbance ( $1 - T$ ) at the excitation wavelength (ESI section S4†). A scaling factor was determined to normalize the most fluorescent monomer sample and then used to scale the remaining samples.

## 2.6. Time-correlated single-photon counting (TCSPC)

Samples for TCSPC (2.8 mL) were prepared such that the absorbance (optical density) using a 1 cm pathlength quartz cuvette (4 mL capacity; Starna) was  $0.05 \pm 0.01$  in a 1 cm pathlength at the excitation wavelength. Data were collected using a Fluorotime 250 (Picoquant; West Springfield, Massachusetts) with a 594 nm wavelength excitation laser (<100 ps pulse). The time-resolved data were fit with one to three exponential functions, as needed, to determine whether multiple time constants were associated with the fluorescence decay. The instrument response function was obtained using a solution of colloidal silica nanoparticles (LUDOX).

## 2.7. KRM modeling

Theoretical modeling was performed using the KRM Model Simulation Tool—an in-house-developed modeling program based on work by Kühn, Renger, and May (KRM).<sup>66</sup> The tool processes experimental absorption and CD extinction data to return the spatial arrangement of the TDMs that reproduce the given spectra, along with providing several other key system parameters. The tool has been previously fully described.<sup>58</sup> In summary, the tool employs a stochastic gradient search to sample TDM orientations that best match the experimental spectra. At each step, the excitonic hopping parameter,<sup>67</sup>  $J_{m,n}$ , is computed using orientation details and experimentally derived magnitudes for the TDMs of participating dyes. Values of  $J_{m,n}$  were calculated using an extended dipole approximation.<sup>68</sup> The  $J_{m,n}$  parameter is used to populate a Holstein<sup>69</sup>-like Frenkel Hamiltonian<sup>70</sup> that is processed to compute the

predicted absorption and CD transition energies, their respective amplitudes, and resulting spectra. We note that the purpose of KRM modeling is to characterize the interactions between the participating TDMs to provide information related to dye-dye coupling and estimates of relative dye-dye orientations without the considerable computational investment (if feasible at all) involved in more complex methods such as time-dependent density functional theory (TD-DFT) or molecular dynamics (MD). Additional modeling details are provided below when warranted and in ESI section S5.†

## 2.8. Nondenaturing polyacrylamide gel electrophoresis (PAGE)

Samples ( $\sim 4$   $\mu$ M, 25  $\mu$ L) were loaded into wells of 10% native PAGE gel (1.5 mm gel thickness; 9 cm length) casted with 1 $\times$  TBE buffer along with 5  $\mu$ L of loading buffer (20% v/v Ficoll [Sigma Aldrich] and 20% v/v bromophenol blue [Sigma Aldrich]). The running buffer was 1 $\times$  TBE, 15 mM MgCl<sub>2</sub> at 22 °C. Samples were allowed to migrate through the gel with 120 V of applied voltage for  $\sim 210$  minutes (3.5 hours). Gels were imaged in a FluoroChem Q imager (Alpha Innotech, San Leandro, California) under *epi*-UV illumination. See ESI section S2† for full gel images and details.

## 2.9. Melting profiles

DNA melting experiments were performed using a Cary-5000 UV-Vis spectrometer (Agilent) using  $\sim 1$   $\mu$ M samples in 1 $\times$  TBE, 15 mM MgCl<sub>2</sub>. Samples were outgassed under vacuum for 5 minutes before loading into a Teflon-capped, low-headspace, 1 cm pathlength quartz cuvette (40  $\mu$ L; Starna). For standard melting experiments, absorption was monitored at 260 nm as temperature was increased from 25 °C to 95 °C (melting) and decreased back to 25 °C (annealing) at a rate of 1 °C min<sup>-1</sup> with data collected every 15 seconds. Variations to this protocol will be detailed later when appropriate. Melting temperatures were determined using the derivative of absorbance with respect to temperature. The peak of each derivative curve was taken to be the temperature for a melting transition (see ESI section S7† for melting profiles and derivatives).

## 2.10. Atomic force microscopy (AFM)

Imaging was performed using a Bruker Dimension FastScan Bio AFM with a FastScan D-SS probe (1 nm radius of curvature,  $k = 0.25$  N m<sup>-1</sup>,  $f_0 \sim 110$  kHz in fluid) in buffer solution using tapping mode (intermittent contact) and a tapping amplitude setpoint relative to free-space of  $A/A_0 \sim 0.85$ . Scan rates of 1.25–2 Hz were employed, depending on image size, with a data acquisition XY resolution of  $\sim 1$  nm  $\times$  1 nm per pixel. Samples were imaged on v1 mica using a protocol adapted from Heenan and Perkins.<sup>71</sup> See ESI section S9† for additional information.

## 2.11. Transient absorption

Femtosecond transient absorption (TA) spectra were collected using a regeneratively amplified Ti:sapphire-based laser system (Coherent Astrella; 5 mJ, 800 nm, 100 fs, 1 kHz).



Approximately 2 mJ of the 800 nm fundamental was directed toward an optical parametric amplifier (Coherent OPERA Solo) to generate a spectrally tunable pump beam. A second portion of the fundamental was directed to a commercial TA spectrometer (Ultrafast Systems, Helios Fire; Sarasota, Florida) to generate a continuum probe (420–760 nm). The pump and probe beams were overlapped at the sample with a relative polarization of 55° (*i.e.*, the magic angle). Samples were loaded into 2 mm pathlength cuvettes (750  $\mu$ L; Starna) with a stir bar. All samples for TA were in 1 $\times$  TBE, 15 mM MgCl<sub>2</sub> and purified by native 10% PAGE. Samples were prepared with optical densities below 0.3 in the visible range. The solutions were stirred during the measurement.

### 2.12. Solid-phase sample preparation and characterization

Solid-phase (dried) samples were prepared by combining equimolar quantities of each component strand in aqueous solution (1 $\times$  TBE, 15 mM MgCl<sub>2</sub>). Samples were annealed by heating to 95 °C and holding for 5 minutes before a linear ramp to 25 °C over  $\sim$ 3.5 hours. Samples (100  $\mu$ L) were transferred by pipette to a clean glass microscope slide cover. Samples were then placed in a closed container at ambient temperature to allow the solvent to evaporate for at least 5 days. Dried samples were placed in the beam path of a Cary-5000 UV-Vis spectrometer (Agilent) and a J-1500 CD spectrometer (JASCO) to record steady-state absorption and CD spectra, respectively. Sample absorption was corrected by subtracting the absorption spectrum obtained from a clean slip-cover. See ESI section S11† for images of dried samples.

## 3. Results and discussion

We present the following results and discussion in order of increasing system complexity. That is, we begin by examining single dyes (monomers) attached to a DX tile (section 3.1). We then proceed by examining the impact of adding multiple dyes with different attachment locations to the tile (sections 3.2–3.3.1). We next elucidate the properties, in terms of both aggregate optical behavior and DNA structural configurations, of higher order (*i.e.*, beyond the original single-tile design) DNA constructs—and their dye aggregates (more than two dyes)—and the implications for assembly of more complex DNA-dye systems (sections 3.3.2–3.3.3). We conclude with transient absorption experiments (section 3.3.4), characterization of solid-phase samples (section 3.3.5), and discussion (section 3.3.6 and General discussion section 4).

### 3.1. Monomers

We characterized eight monomer constructs to assess DNA-dye behavior when the dye is incorporated at any of several positions on a DX-DAE tile with 21 base pairs (bp; four half-turns of the DNA double-helix) between crossovers. Dyes were attached to modified nucleobases *via* a single covalent linker (Fig. 1a), with the DNA sequences of each strand otherwise held constant. Monomer-modified bases were positioned

between the crossover junctions of the tile on the un-nicked duplex (Fig. 1b and 2).

**3.1.1. Steady-state absorption and fluorescence.** Monomer constructs were first characterized by UV-Vis absorption. Monomer absorption spectra were typical of squaraine dyes and comparable to previous work with SQ-Cl<sub>2</sub> templated by an immobile HJ.<sup>42,43,60</sup> The spectra consisted of strong 0–0 absorption bands with relatively weak vibronic progressions (Fig. 3). The Huang–Rhys factor,<sup>72</sup> a measure of coupling to vibrational modes, was estimated using the KRM Model Simulation Tool (Table 1) for each sample. Constructs **M1–M6** exhibited absorption maxima between 638 nm and 641 nm. Notably, monomer constructs **M7** and **M8** had absorption maxima that were red-shifted to 645 nm and 649 nm, respectively.

Steady-state fluorescence spectra were collected from each sample and are shown in Fig. 4. The spectra generally resembled mirror images of the absorption spectra, with consistent Stokes shifts of  $27 \pm 3$  meV ( $220 \pm 20$  cm<sup>−1</sup>). Monomer constructs **M1–M6** had fluorescence maxima between 648 nm and 650 nm, whereas monomers **M7** and **M8** were again red-shifted relative to the other samples, with maxima at 653 nm and 659 nm, respectively.

When corrected for sample absorbance at the excitation wavelength (635 nm) and then scaled relative to each other, the monomer fluorescence spectra revealed significant differences in relative fluorescence intensities (Fig. 4). Monomer **M8** had the highest relative fluorescence intensity. Therefore, the fluorescence of all other samples in this study were analyzed relative to **M8**. Monomer constructs **M1–M6** had similar intensities relative to each other, with **M1** and **M3** being the most intense of the group. Monomers **M7** and **M8** had the highest relative intensity, with **M8** showing a roughly two-fold increase in scaled intensity compared to the least-fluorescent monomer (**M6**).

**3.1.2. Time-correlated single-photon counting (TCSPC).** To further characterize the fluorescence behavior of select representative monomers, TCSPC experiments were performed on constructs **M6** (least-), **M7** (intermediate-), and **M8** (most-fluo-

**Table 1** Summary of steady-state absorption (Abs.) maximum, fluorescence (Em.; 635 nm excitation) maximum, Stokes shift, Huang–Rhys factor, and TDM magnitude for monomer constructs **M1–M8**

Sample <sup>a</sup>	$\lambda_{\text{max}}$ Abs. [nm]	$\lambda_{\text{max}}$ Em. [nm]	Stokes shift [meV]	Huang–Rhys factor <sup>b</sup>	TDM <sup>b</sup> (D)
<b>M1</b>	638	648	30	0.23	12.68
<b>M2</b>	639	648	27	0.23	12.33
<b>M3</b>	640	648	24	0.22	12.37
<b>M4</b>	640	650	30	0.25	12.26
<b>M5</b>	641	650	27	0.25	12.46
<b>M6</b>	640	649	27	0.25	12.32
<b>M7</b>	645	653	24	0.25	12.62
<b>M8</b>	649	659	29	0.24	13.23

<sup>a</sup> All samples in 1 $\times$  TBE, 15 mM MgCl<sub>2</sub>; 10% native PAGE purified (see ESI section S2† for gel images). <sup>b</sup> Huang–Rhys factor and TDM magnitude estimated from KRM modeling. See ESI section S5.†



**Table 2** TCSPC results for select monomer samples (**M6**–**M8**)

Sample <sup>a</sup>	$\tau_1$ <sup>b</sup> [ns]	$\tau_2$ <sup>b</sup> [ns]	$\tau_{\text{avg}}$ <sup>c</sup> [ns]	$\frac{\Phi_{\text{F}}}{\Phi_{\text{F,M8}}}$ <sup>d</sup>	$\frac{k_{\text{rad}}}{k_{\text{rad,M8}}}$ <sup>d</sup>
<b>M6</b>	2.30 (45%)	1.13 (55%)	1.66	0.39	0.64
<b>M7</b>	2.57 (78%)	1.23 (22%)	2.28	0.68	0.81
<b>M8</b>	2.85 (91%)	1.27 (9%)	2.70	1	1

<sup>a</sup> All samples were prepared in 1× TBE, 15 mM MgCl<sub>2</sub>. <sup>b</sup> Data for each sample were fit using a two-exponential decay model with time constants  $\tau_1$  and  $\tau_2$ , each with associated amplitudes and relevant percent contribution (see ESI section S4† for raw data, uncertainty estimates, and fits). <sup>c</sup> Amplitudes were used to determine the amplitude-weighted average ( $\tau_{\text{avg}}$ ; ESI section S4†). <sup>d</sup> Ratios of fluorescence quantum yield  $\Phi_{\text{F}}$  and radiative decay rates  $k_{\text{rad}}$  were determined relative to sample **M8** (see ESI section S4† for information related to these calculations).

rescent). Fluorescence decay data for each monomer were well-described by fitting with two time-constants with differing relative amplitudes. Each construct was fit with a longer (~2.6 ns) and shorter (~1.2 ns) time constant (Table 2). The excited-state lifetimes of each monomer were estimated using the amplitude-weighted average of the two time constants. Monomer excited-state lifetimes progressively increased from 1.66 ns (**M6**) to 2.70 ns (**M8**) as the relative amplitude of the longer time component increased relative to the shorter component. A plausible interpretation of this observation is that **SQ-Cl<sub>2</sub>** existed as two conformers with different lifetimes, and that samples **M7** and **M8** were biased toward the longer-lifetime conformer. The observed increase in monomer lifetimes corresponds to the observed shifts to longer absorption and emission wavelengths and increased fluorescence intensity.

Steady-state absorption and fluorescence data were used in conjunction with TCSPC data to estimate the relative fluorescence quantum yield,  $\Phi_{\text{F,r}}$  and radiative decay rate,  $k_{\text{rad,r}}$  for each construct relative to **M8** (see ESI section S4† for details regarding calculations). Monomer **M6** was found to have the lowest  $\Phi_{\text{F,r}}$  and  $k_{\text{rad,r}}$ . Monomer **M7** had values intermediate to **M6** and **M8**, with **M8** having the highest  $\Phi_{\text{F}}$  and  $k_{\text{rad}}$ , again corresponding with progressive red-shifts in absorption and emission maxima and increased excited-state lifetimes.

**3.1.3. Partial tile and monomer dry experiments.** Because each monomer construct had the same material components apart from the differing bases used to tether each dye, it stands to reason that variations in the local DNA environment at the final resting place of the dye were responsible for the differences in observed properties. To understand the role of the local DNA environment, we removed selected strands in such a manner that would modulate the structure of the crossover while maintaining the same DNA bases surrounding the dye anchoring point. A partial tile was prepared using four of the five strands so that the crossover nearest the dye attachment was not fully formed (Fig. 5a and b). Additional samples were prepared using only the dye-labeled strand (single-stranded [ss]DNA) and another including the central strand that hybridized with the dye-labeled strand in the region where the dye was attached (double-stranded [ds]DNA).

Absorption spectra were collected for each variant of **M8** and compared with construct **M8** (Fig. 5c). All variants had absorption maxima at 645 nm, whereas construct **M8** absorbed with a maximum at 649 nm.

To gain further insight into sample **M8**'s behavior, **M8** and its variants were each transferred to a glass slide and allowed to dry into a solid-phase film. Examining these constructs in the solid phase not only provided insight into the behavior of the dye in sample **M8**, but also served as a reference to compare to solid-phase absorption of aggregates (see section 3.3.5). Steady-state absorption was collected from each dry sample and compared with absorption from **M8** in solution (Fig. 5d). In solid phase—as with **M8** in solution—every construct exhibited an absorption maximum at 649 nm. Unsurprisingly, ssDNA and dsDNA samples showed an increase in absorption at the 0–1 transition consistent with dye dimerization, indicating a propensity for the dyes to aggregate during the drying process. Dye aggregation during drying is likely due to increasing DNA and salt concentrations as the solvent evaporates, enabling exposed dyes to come into direct contact. Interestingly, the partial tile and full **M8** construct did not show an increase in the 0–1 vibronic feature, suggesting that the dyes were embedded in the DNA such that they were unable to aggregate upon drying. We note that the absorption line-shape of the full **M8** construct was essentially unchanged upon going from solution to solid phase.

**3.1.4. Discussion.** The observed differences in optical properties arising from the covalent attachment of dyes to different nucleobases in the DX tile are worth consideration. Because the DNA sequences for each of our samples were identical apart from the functionalized nucleobase, it follows that the resulting properties were primarily dependent on the local DNA-solvent environment surrounding each dye in its final configuration. It is a reasonable hypothesis that the extended single-linkers used here to covalently attach the dyes to the tile allowed significant freedom for dyes to sample a variety of locations on the tile in search of an energetically favorable environment; however, the observed properties can still provide insight regarding the specific DNA–dye configuration of each sample.

In constructs **M1**–**M6**, the dyes were covalently attached to the un-nicked domain of the tile—with the linker extending from the edge of the major groove of the double-helix—such that the modified nucleobases were ≥7 bp (≥2 nm along the helical axis) from a crossover junction, whereas the length of the carbon-based linkers used to attach each dye was estimated to be 1.7–2.1 nm when fully extended with typical bond-angles (ESI section S6†). Therefore, the effective linker length would not be expected to allow the dyes in samples **M1**–**M6** to reach the crossover junction based on their attachment points (Fig. 2). Thus, it follows that the dyes in samples **M1**–**M6** were distributed along the DNA helix between the two crossovers; however, their specific DNA–dye configuration is still unclear. In general, small molecules such as hydrophobic dyes can interact with DNA *via* at least two principal modes: intercalation and groove-binding.<sup>59</sup>



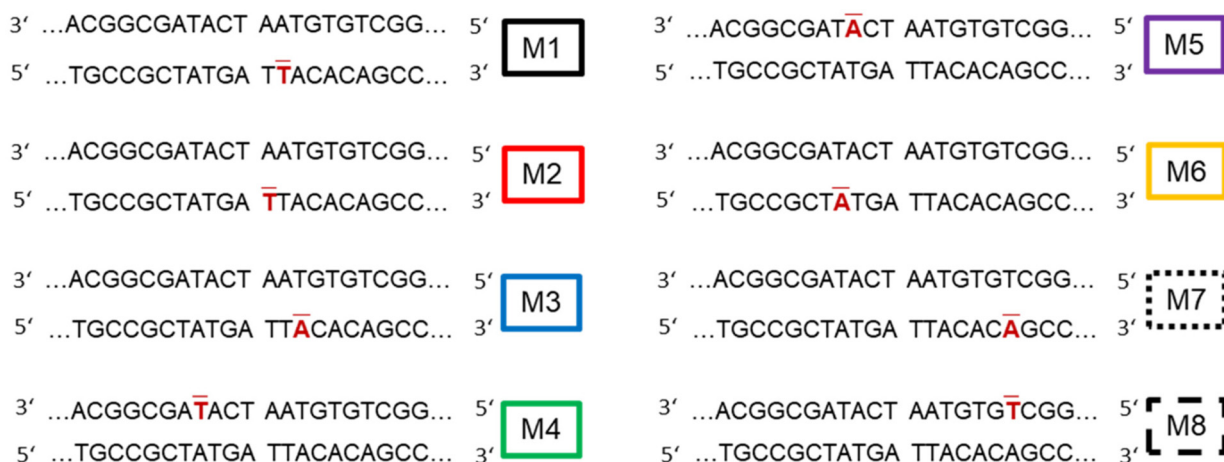


**Fig. 2** Sequences detailing the locations of dye-modified bases for monomer samples **M1–M8**. Dye-modified bases are marked in red with an overbar. Sample names are outlined with colors corresponding to later plots.

Intercalation refers to a planar dye inserting into the DNA stack between two nucleobases, which requires that the DNA lengthen and unwind to accommodate the dye.<sup>59,73</sup> This mode was unlikely for samples **M1–M6** because the required distortion of the DNA—*i.e.*, unwinding to create space ( $\sim 0.34$  nm) for an intercalated dye—in the central domain of the tile was suppressed by the design of the tile that couples the bending, twisting, and unwinding modes to the adjacent DNA duplex (Fig. 1b). That is, the unwinding of a base pair—to accommodate intercalation—in the central domain (between the crossovers) would result in an unfavorable alignment of the duplexes at the crossover due to the additional length and reduced helical twist of the duplex hosting the intercalated dye relative to the adjacent duplex. Instead, it is likely that the dyes in samples **M1–M6** were externally bound to the DNA, most likely in the minor groove.<sup>59</sup> Groove binding is supported by the observation of a red-shifted absorption maximum as compared with the spectrum of the free dye in methanol (Fig. 3). The differences in absorption maxima and relative fluorescence in **M1–M6** were likely the result of subtle differences in specific electrostatic interactions with the different nucleobases within the DX tile sequence local to the dye attachment location (*i.e.*, within the range of the linker) or other aspects of the local environment. Determining the precise location of the dyes in every monomer sample is beyond the scope of the current study but could be ascertained by advanced characterization methods including single-molecule approaches or nuclear magnetic resonance (NMR).

In contrast to samples **M1–M6**, samples **M7** and **M8** were templated within 4 bp ( $\sim 1.35$  nm) of one of the crossover junctions; thus, the dyes in samples **M7** and **M8** could—in principle—have enough freedom imparted by their respective linkers to reach the crossover and (at least) partially intercalate<sup>74</sup> into the DNA bases at the crossover. The observed differences in optical properties for samples **M7** and **M8** compared to **M1–M6** support the mechanism of intercalation. Samples **M7** and **M8** were incrementally red-shifted from the other

samples consistent with their relative proximity to the nearest crossover; that is, **M8** is attached closest to the crossover and utilized a linker that was three carbons longer than sample **M7** (Fig. 1a [linker schematics] and 2 [attachment base location and identity]), which presumably allowed additional freedom for the dye to insert into the crossover. The linker from sample **M7** extended from the opposite side of the duplex with a shorter linker than sample **M8** (Fig. 1a), but still roughly within range of the crossover. This perhaps enabled partial intercalation at the crossover, consistent with the intermediate absorption maximum and fluorescence amplitude relative to samples **M1–M6** and sample **M8** (Fig. 3 and 4b).

The bathochromic (red) shifts in absorption maxima for samples **M7** and **M8** were consistent with expected effects arising from intercalation of dyes into a DNA base stack, though it can be challenging to assign the shifting to specific mechanisms. Asanuma and coworkers<sup>75</sup> summarize several possible explanations for the shifts in absorption wavelength. One possibility—and most likely the dominating mechanism in our system—is that the observed red-shifts were a result of differing polarizability of the local environment surrounding the dye.<sup>76</sup> Symmetric squaraine dyes in general are known to be weakly solvatochromic,<sup>77</sup> though the effect of solvent polarity is dependent on the specific substituents of individual dye species. A second possibility that can lead to red-shift in absorption maxima is that intercalated (as well as groove-bound) dyes may experience a redistribution of electron density due to electrostatic interactions with the negatively charged phosphate backbone, resulting in a decrease in the energy gap between the HOMO and LUMO levels in the dye and a corresponding red-shift in absorption relative to non-intercalated or unbound dyes.<sup>78</sup> This mechanism is likely to be at work to some degree in all samples and may account for the subtle differences in absorption maxima for the presumed groove-bound samples (**M1–M6**).

In this work, we note that we also observed a slight increase in absorption intensity (*i.e.*, hyperchromicity) for sample **M8**



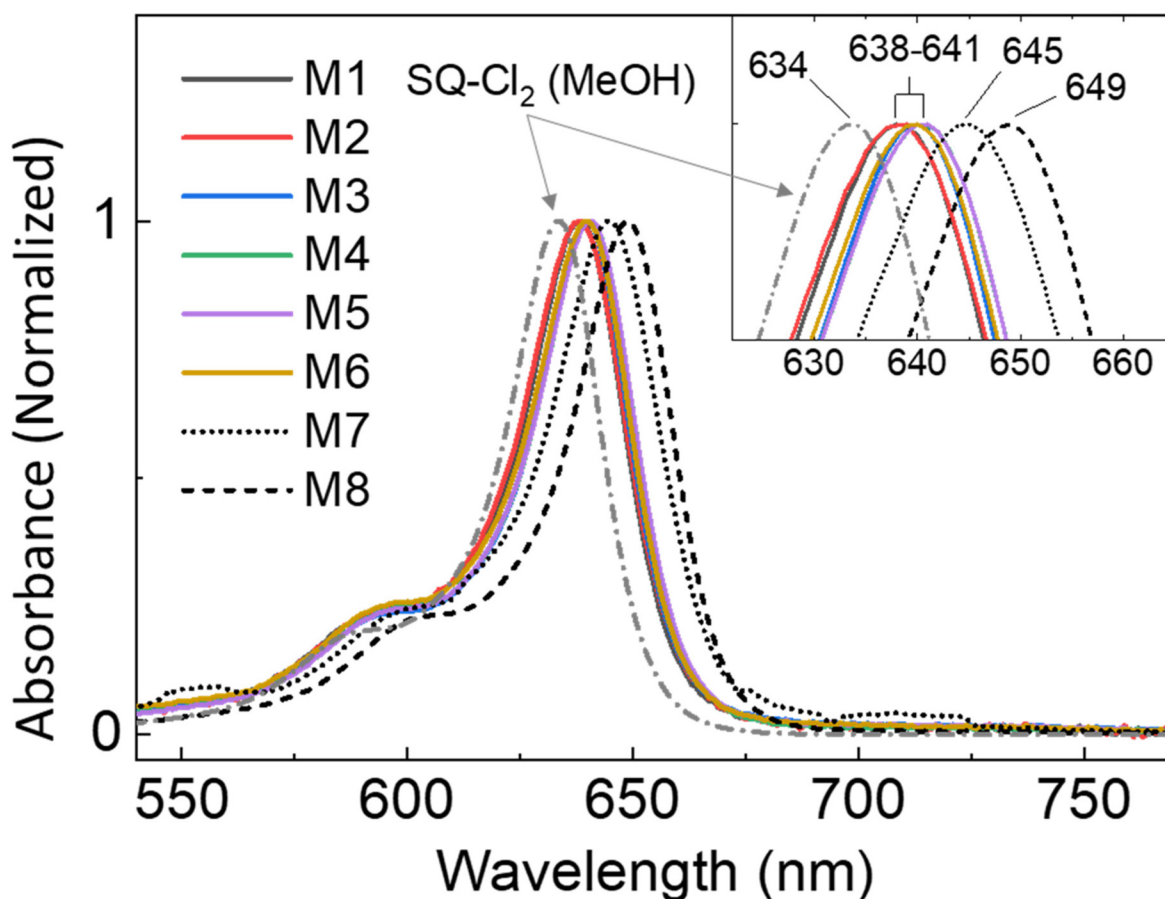


**Fig. 3** Normalized absorption spectra of monomer constructs (M1–M8). The absorption spectrum of the free dye in methanol (MeOH) is provided as reference. The inset provides a magnified view of peak positions (see also Table 1). Monomer constructs M7 and M8 are distinguished by dotted and dashed lines, respectively. All samples were prepared in 1x TBE, 15 mM  $\text{MgCl}_2$ ; 10% native PAGE purified (see ESI section S2† for gel images).

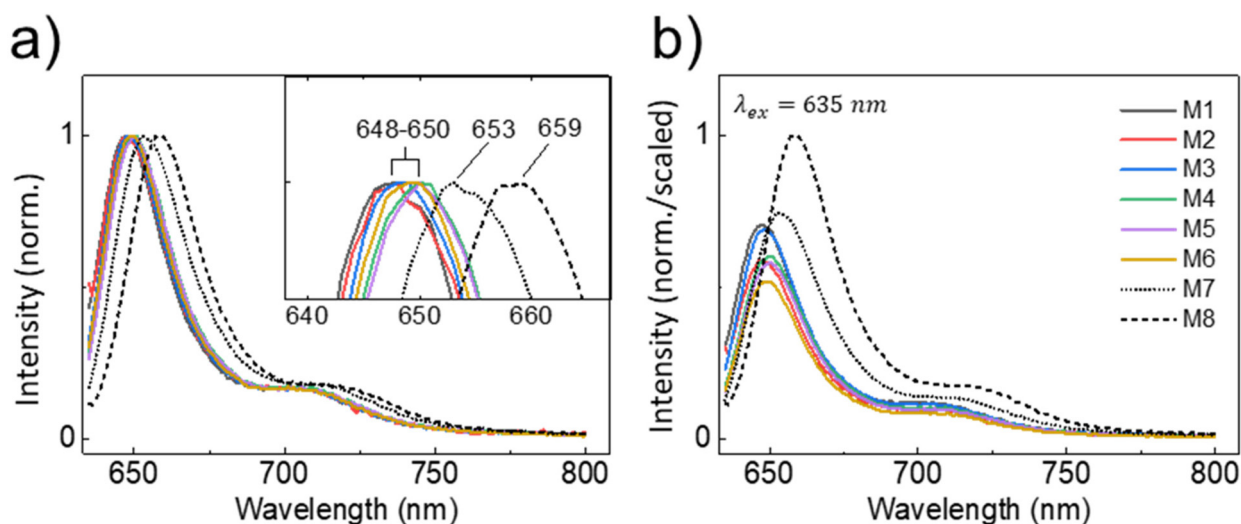
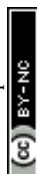


**Fig. 4** Steady-state fluorescence emission (635 nm excitation) of monomer constructs M1–M8 (a) normalized and (b) normalized and scaled. Scaled data were processed by first adjusting for the absorbance of each sample at the excitation wavelength and then scaling each curve using a normalization factor determined for the brightest sample (M8; ESI section S4†). Constructs M7 and M8 are distinguished by dotted and dashed lines, respectively. The inset in the left panel shows peak positions (see also Table 1). All samples were prepared in 1x TBE, 15 mM  $\text{MgCl}_2$ ; 10% native PAGE purified (see ESI section S2† for gel images).



(ESI section S3†). The increased absorption was consistent with previously reported TD-DFT results showing that the **SQ-CL<sub>2</sub>** dye can adopt either a *cis*- or *trans*-conformation, with the latter having a slightly larger TDM magnitude.<sup>64</sup> Interestingly—in combination with our TCSPC results—this suggested that the **M8** dye favored the *trans*-conformation. Conversely, the *cis*-conformation may be more conducive to groove binding due to this conformation's geometric fit with the curvature of the DNA (minor) groove.<sup>59,64</sup>

Free squaraines are also known to photoisomerize leading to non-radiative relaxation<sup>79</sup> (quenching) and reduced excited-state lifetimes.<sup>77,80</sup> Additionally, the bi-exponential decay in the time-resolved fluorescence (Table 2) suggested that the dyes may exist in multiple conformations in solution, and that **M8** was heavily biased toward a conformation with a relatively long excited-state lifetime and higher  $\Phi_F$ . It is reasonable to

conclude that steric hinderance from intercalation into the DNA bases at the crossover in **M8** suppresses non-radiative decay by restricting photoisomerization leading to increased  $\Phi_F$  and a longer excited-state lifetime.

The observations of increased fluorescence intensity and extended lifetime of sample **M8** support the mechanism of intercalation. Intercalation was further supported by the partial-tile experiments in which the red-shift was only realized when the full tile, including the nearby crossover, was completely formed. Solid-phase experiments also showed that all **M8** variants absorbed at the same wavelength when the aqueous solvent was removed, suggesting that sample **M8** effectively isolated the intercalated dye from the solvent, whereas the partial-tile variants allowed some exposure to the aqueous solvent that was eliminated upon drying. Unfortunately, common methods to confirm intercalation in free-dye-DNA

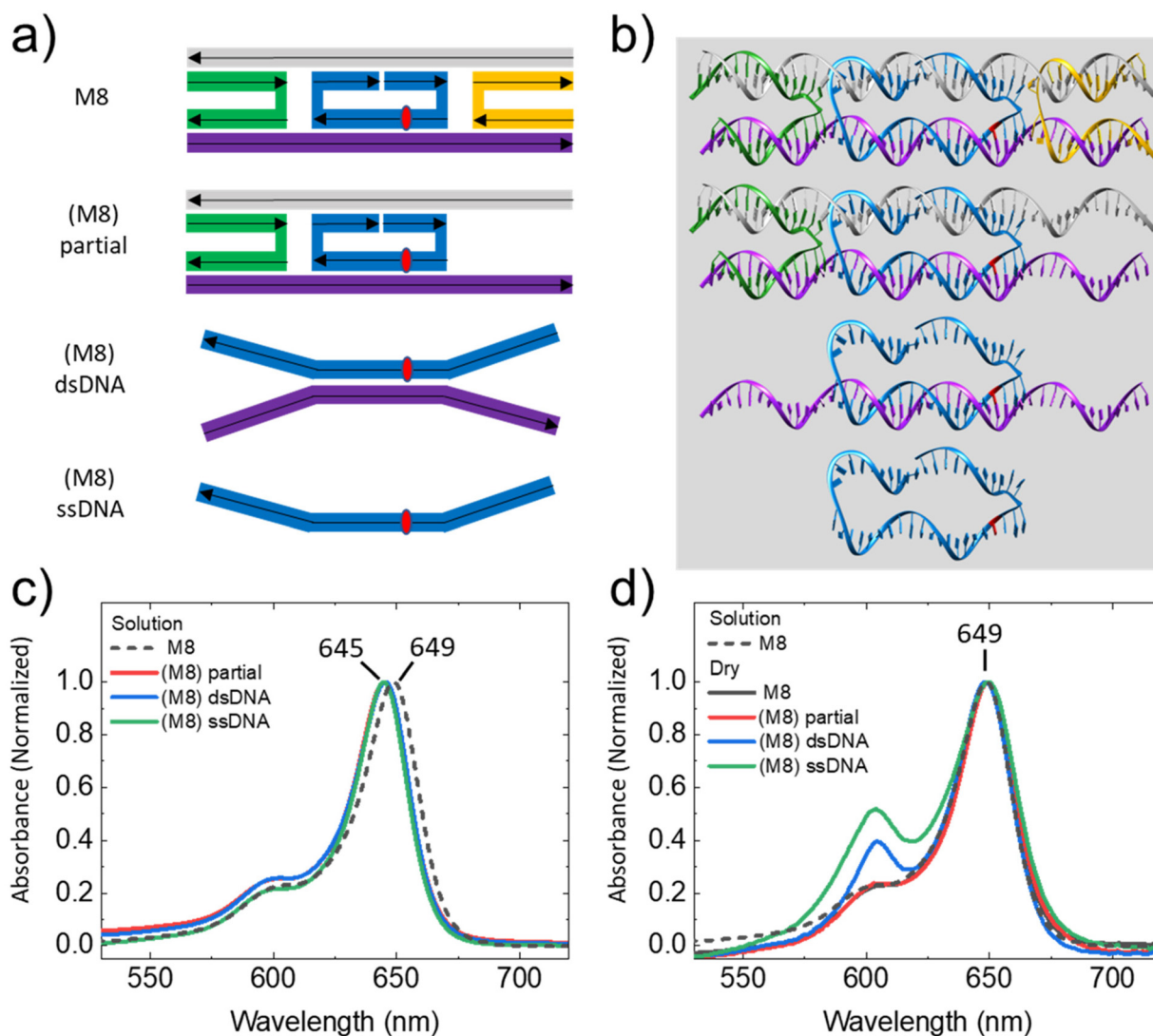


**Fig. 5** (a) Schematics and (b) DNA template images of sample **M8** and variations using a partial tile, dsDNA, and ssDNA. (c) Normalized absorption spectra of **M8** and variants in solution. (d) Normalized absorption spectra of **M8** and dried variants. The spectrum of **M8** in solution is repeated for comparison. Solution samples were prepared in 1× TBE, 15 mM MgCl<sub>2</sub>.



systems, such as detecting increased melting temperatures from DNA stabilization or perturbations to DNA-associated CD features, are not practical in this case because a single dye would be expected to have minimal effect on the overall melting temperature or CD signal from the DNA in the DX tile. Although unambiguous determination of intercalation is a challenge, in combination, these preceding lines of indirect evidence led us to conclude that the dye in sample **M8** was intercalated into the DX tile at one of the crossover junctions and that sample **M7** was partially intercalated.

### 3.2. Dimers: two dyes attached to a single strand within a DX tile

The previous section detailed differences in optical properties and excited-state dynamics of monomeric dyes that were strongly dependent on the linker attachment point on the DNA template and ultimately the final dye location relative to the DNA structure and interaction mode with the DNA. Adding dyes to the system is likely to impact these interaction modes due to the highly interactive nature of the dyes themselves. As a result, further development of DNA-dye systems that utilize induced dye aggregation for exciton delocalization requires an understanding of the factors affecting these aggregates—and their integration with the DNA template—with a focus on controlling the number of dyes, their relative separation and orientation, and their location within the DNA template. The fundamental building block for aggregate-based excitonic systems is the dye-dimer. The following section surveys the steady-state optical properties of 16 distinct dimer designs, each composed of two dyes templated to a single strand within the DX tile—again in the region between the crossovers on the un-nicked helix—but with 0–3 bp separations between attachment points. This set of designs further illustrates the diversity in local DNA-dye interactions—and resulting optical properties—available to dyes templated on the interior domain of the DX tile and their potential applications.

**3.2.1. Steady-state absorption, circular dichroism, and fluorescence.** A primary consideration for aggregated dimers is to quantify the degree of coupling between their TDMs—represented by  $J_{m,n}$ <sup>41</sup>—as this is an important measure of the strength of exciton interaction. In general, monomers in close proximity can interact through their TDMs with a resultant change of electronic structure and redistribution of oscillator strength in the absorption spectrum that is dependent on their TDM geometries. In the absence of other forces, squaraines and other planar dyes tend to form H-like (co-facially stacked) dimers<sup>37,41,42,60</sup> with increased absorption near the 0–1 monomer transition (“peak 1”) and a decrease at the 0–0 monomer transition (“peak 2”). As a first-order measure of coupling strength, one can consider the absorption peak-height ratio between features in the 0–1 and 0–0 wavelength regions. To simplify notation in the text, we will refer to this ratio as the 0–1/0–0 ratio. Although this view is convenient from survey and comparison perspectives, it should be approached cautiously because sample heterogeneity (in terms of DNA structure or dye-dye geometry) can obfuscate interpretation. Additionally, in our study, dimers templated to two

different bases on a single DNA strand had significant variation across their absorption characteristics (Fig. 6 and 7; Table 3).

With the above limitations in mind, the ratios for dimer constructs are presented in Table 3. Different dimer designs exhibited a significant range of ratios, as well as notable differences in the wavelength of their absorption maxima, ranging from nearly monomeric behavior (e.g., **D6**) to spectra that suggested strongly coupled dimers. In general, dimers templated to the central strand (Fig. 1b) were less strongly coupled than those templated on the complementary linear strand (Fig. 6 and 7; Table 3). Additionally, with the exception of **D7**, dimers on the linear strand with one or two natural (unmodified) base-pair(s) between dye attachment points resulted in higher 0–1/0–0 ratios relative to their consecutive-base templated counterparts. Dimers with three base-pairs between attachment points generally exhibited lower ratios and potential aggregate heterogeneity (*i.e.*, subpopulations of aggregates with differing geometry) compared with other dimer designs.

Steady-state fluorescence revealed that all dimer constructs were significantly quenched relative to the monomeric dye. The fluorescence spectra generally resembled the mirror image of the monomer absorption spectra. Fluorescence maxima ranged from 648 nm to 653 nm, with differing relative amplitudes (Fig. 6c and 7c). Relative fluorescence data are represented as normalized and scaled emission amplitudes in Table 3 with data scaled relative to monomer **M8**. Scaled emission amplitudes of dimer constructs were generally less than 0.1, with two exceptions—**D4** and **D6**—both of which had 0–1/0–0 ratios less than unity; that is, the majority of their absorption was near the 0–0 monomer transition wavelength. Scaled emission amplitudes of dimer constructs were generally inverse to the observed 0–1/0–0 ratios; that is, the relative emission amplitudes decreased as the 0–1/0–0 ratio increased.

Circular dichroism spectra from this high-throughput dimer survey were largely featureless in the wavelength range corresponding to dye absorption (Fig. 6b). An absence of CD features corresponding to absorption transitions in excitonically coupled dimers can be interpreted as (1) a planar (achiral) alignment of TDMs of the interacting dyes or (2) a mixture of dimer arrangements with similar absorption characteristic but opposite handedness (enantiomers) that produce competing CD signals that effectively cancel each other.<sup>38,63</sup> We note that the CD spectra shown in Fig. 6b and 7b were collected from low-concentration, gel-purified samples, and that underlying CD features may be below the noise level of the instrument. Indeed, further characterization of dimer **D7** with optimized sample conditions revealed subtle CD features (Fig. 8a).

**3.2.2. Discussion.** Due to the tendency of hydrophobic squaraine dyes to stack co-facially,<sup>39,41,42,60</sup> an additional measure that can inform both coupling (*i.e.*, coupled *versus* un-coupled dyes) and sample heterogeneity is relative fluorescence suppression (*i.e.*, quenching). Close-packed H-like dimers are generally quenched relative to their monomeric forms owing to increased non-radiative decay<sup>35,81</sup> and the selection rules arising from symmetry arguments and applying



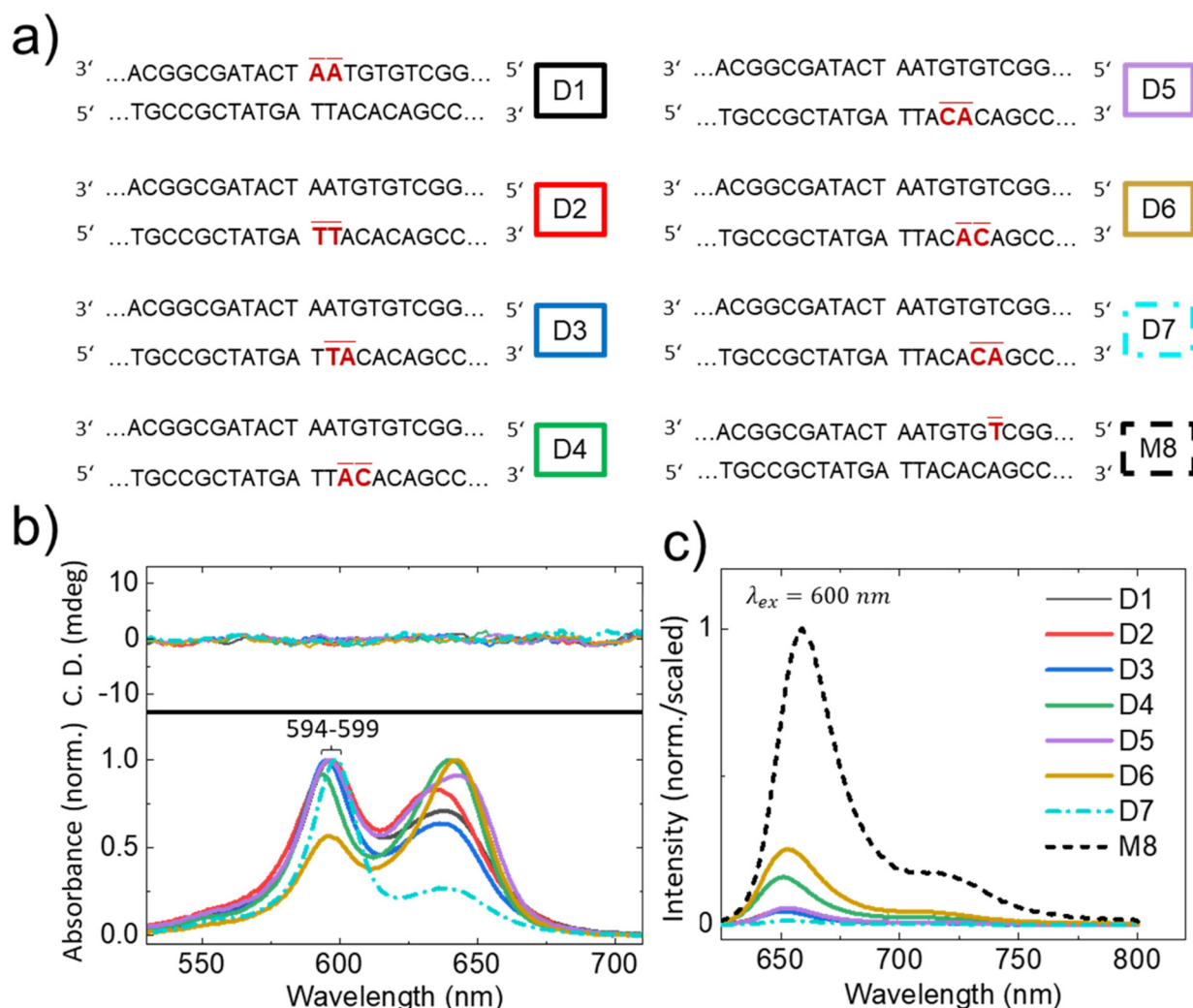
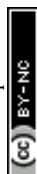


**Fig. 6** (a) Sequences detailing locations of dye-modified bases for dimer samples **D1–D7**, all of which have a 0 bp separation between dye attachment locations. Monomer **M8** is repeated for reference. Dye modified bases are marked in red with an overbar. Sample names are outlined with colors corresponding to later plots. (b) Normalized absorption and CD (mdeg) spectra for samples **D1–D7** (see ESI section S3† for individual plots). (c) Steady-state fluorescence emission of dimer samples **D1–D7**. All fluorescence was scaled relative to monomer **M8** by determining a normalization factor for **M8** and applying it to all samples. All samples were prepared in 1x TBE, 15 mM  $\text{MgCl}_2$ , 10% native PAGE purified (see ESI section S2† for gel images).

Kasha's rule.<sup>82</sup> Additionally, sample heterogeneity—including subpopulations of aggregates or the presence of monomeric dyes<sup>81</sup>—can be expected to increase fluorescence compared to ideally stacked, homogeneous dimers. Although the origin of any observed fluorescence is difficult to ascertain, samples with dimers showing relatively low fluorescence are likely to be composed of dimer populations with minimal orientational variation or monomer contamination. Thus, with caution, we posit that a high 0–1/0–0 ratio combined with high fluorescence quenching can inform the degree of dye–dye coupling and possible presence (or lack) of aggregate subpopulations in H-like aggregates. We note that here we use the term “subpopulations” to refer to different configurations of dyes—which could include monomer content—to distinguish this form of sample heterogeneity from differences in DNA configuration, which we will refer to as structural heterogeneity.

For this study, we were most interested in designs that produced robust, strongly coupled, and homogeneous aggregate populations. Somewhat surprisingly, dimers with dyes attached to consecutive bases were not generally the most well-behaved. In general—with the exception of **D7** (discussed below)—these serial dimers exhibited complex absorption line shapes with substantial oscillator strength remaining near the 0–0 monomer transition wavelength. Combined with relative fluorescence data, we infer that significant subpopulations of monomers were present in the **D4** and **D6** samples; however, the increased quenching observed for dimers **D1–D3** and **D5** suggested that their spectra resulted from multiple subpopulations of low-fluorescence dimers or subpopulations of monomeric dyes.

In contrast to consecutively templated dimer designs, dimers with one or two natural (unmodified) base pairs



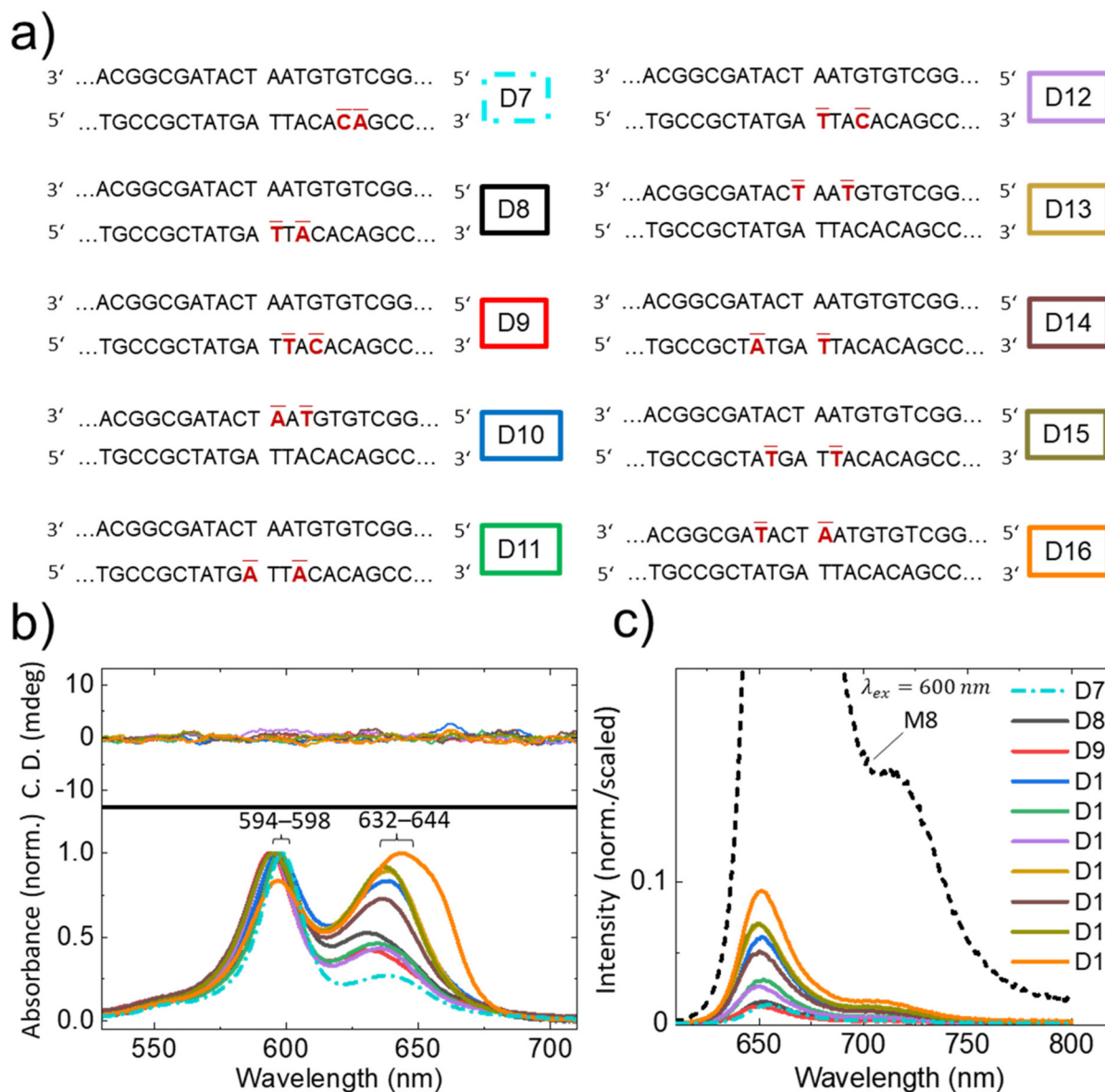


**Fig. 7** (a) Sequences detailing locations of dye-modified bases for dimer samples D7–D16. Monomer M8 is repeated for reference. Dye modified bases are marked in red with an overbar. Sample names are outlined with colors corresponding to later plots. (b) Normalized absorption and CD (mdeg) spectra for samples D7–D16 (see ESI section S3† for individual plots). (c) Steady-state fluorescence emission of dimer samples D7–D16. All fluorescence was scaled relative to monomer M8 by determining a normalization factor for M8 and applying it to all samples. All samples were prepared in 1× TBE, 15 mM MgCl<sub>2</sub>, 10% native PAGE purified (ESI section S2†).

between dye-modified bases—specifically those templated to the central strand—tended to have higher 0–1/0–0 ratios and lower relative fluorescence amplitude, implying strong exciton delocalization and minimal monomer subpopulation contamination. Additionally, we note that the reduced amplitude and width of absorption features near the monomer absorption maximum implied that dimers with separated attachment points have reduced variation (*i.e.*, subpopulations) in dimer geometry relative to consecutively attached dimers.

We note that all dimers with three natural base pairs between dye-modified bases exhibited relatively low 0–1/0–0 ratios. We surmise that the dyes are unable to efficiently

couple at this distance owing to the limits of the length of the linkers to the DNA, wherein both the linear distance along the DNA helical axis ( $\sim 1.4$  nm) and the rotation around the double-helix ( $\sim 140^\circ$ ) must be accounted for. As a result, the two dyes and their linkers would be required to span an estimated 4 nm distance to dimerize. Assuming the expected DNA conformation, the dye linkers may be expected to exit the major groove of the helix on opposite sides of the DX tile for some designs, thus decreasing the probability of forming a homogeneous dimer population.

From this high-throughput survey of dimer designs (Table 3), we conclude that the most intriguing dimer from

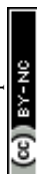


**Table 3** Summary of steady-state optical properties for dimers **D1**–**D16** organized by base-pair separation, including absorption and emission maxima, the ratio between the primary aggregate absorption feature (peak 1) and the feature near the monomer wavelength (peak 2), and the normalized and scaled emission amplitude

Sample <sup>a</sup>	Base-pair separation of attachment	$\lambda_{\text{max}}$ Abs. [nm]	$\lambda_{\text{max}}$ Em. [nm]	Peak 1/peak 2 Ratio	Norm/scaled Em. amplitude
<b>D1</b>	0	596	653	1.43	0.054
<b>D2</b>	0	597	650	1.20	0.048
<b>D3</b>	0	595	651	1.57	0.046
<b>D4</b>	0	641	651	0.92	0.162
<b>D5</b>	0	596	653	1.10	0.057
<b>D6</b>	0	642	653	0.57	0.256
<b>D7</b>	0	599	653	3.70	0.013
<b>D8</b>	1	594	652	1.90	0.015
<b>D9</b>	1	594	651	2.38	0.012
<b>D10</b>	1	597	651	1.20	0.061
<b>D11</b>	2	597	652	2.16	0.031
<b>D12</b>	2	595	648	2.32	0.026
<b>D13</b>	2	595	650	1.11	0.070
<b>D14</b>	3	595	650	1.37	0.051
<b>D15</b>	3	595	649	1.09	0.071
<b>D16</b>	3	644	651	0.84	0.093

<sup>a</sup> All samples were prepared in 1× TBE, 15 mM MgCl<sub>2</sub>; 10% native PAGE purified (see ESI section S2† for gel images).

this set for further study—*i.e.*, the one with the highest 0–1/0–0 ratio, a low relative fluorescence amplitude (<0.02), and exhibiting the least evidence of sample heterogeneity (*i.e.*, most homogeneous)—is the **D7** dimer. We chose the **D7** design for more advanced characterization *via* KRM modeling (following section), transient absorption (section 3.3.4), and transfer to solid phase (section 3.3.5) to demonstrate its robust, reproducible, and seemingly homogeneous properties.

**3.2.3. KRM modeling of D7.** To further investigate the excitonic coupling in the **D7** dimer, we modeled its UV-Vis absorption and CD spectra using our KRM Model Simulation Tool (see Methods). The **D7** dimer was modeled as a single homogeneous population of dimers with a close-packed (<5 Å separation), face-to-face (H-like) geometry. Model results showed that TDMs were nearly co-planar and parallel with a small twist angle,  $\theta_t$ , of less than 4 degrees and a total angle (in three dimensions),  $\alpha$ , of less than 10 degrees between the TDM vectors (Fig. 8d). The modeled exciton coupling of 116.7 meV (941 cm<sup>−1</sup>) is comparable with the highest coupling reported to date for a DNA HJ-templated singly linked squaraine dimer<sup>42,60</sup> and three-fold higher than DFT-derived excitonic couplings recently reported for DNA-templated, double-linked squaraines.<sup>62</sup> Fig. 8 summarizes key outputs for **D7**, including  $J_{m,n}$  and orientation parameters such as the center-to-center TDM separation,  $R_{m,n}$ , and the relative angles between the TDMs. See ESI section S5† for complete modeling details.

Squaraine dyes are known to undergo complex photophysics that are not considered in the KRM model. These effects include non-negligible quadrupole interactions<sup>83</sup> for some dimer geometries arising from the zwitterionic nature of the dye and potential charge-transfer interactions.<sup>84</sup> Although our KRM model does not explicitly consider quadrupole or charge-

transfer interactions, experimental absorption and CD spectra of dimer **D7** were adequately (absorption and CD overlap integrals [ $O_{\text{I}_{\text{ABS}}}$  and  $O_{\text{I}_{\text{CD}}}$ ] > 0.9; see ESI section S5, Table S9†) captured by modeled spectra of a single population of TDM orientations (Fig. 8). For the modeled orientation, quadrupole effects should be negligible compared with dipole interactions.<sup>83</sup> Moreover, our KRM results suggested it was not necessary to invoke charge transfer to describe the aggregate behavior of dimer **D7**. In summary, our results demonstrated the utility of the **D7** design to produce homogeneous dimer aggregates with strong exciton coupling.

### 3.3. Opposed dimers and higher-order constructs

The previous section investigated aggregate behavior for dimers in which both dyes were attached to a single strand within the DX tile. Somewhat surprisingly, a wide range of properties and coupling behavior were observed arising from translating (moving the positions of) the linker attachments along the DNA double-helix. The final properties of the system were ultimately influenced by the local DNA environment surrounding the final resting place of the dimer or individual dyes rather than primarily by the nearest neighbor bases as one might expect with double-linker phosphoramidite inclusions.<sup>85</sup> Dimer behavior was unintuitive in that dyes that were attached to adjacent bases were not necessarily more strongly coupled than their separated counterparts. We attribute this variation to the freedom imparted by the long linker to find an energetically favorable environment within the DNA. Furthermore, we found that dyes and dimers that were templated within range of a crossover junction showed the most desirable properties, suggesting that the increased flexibility of the crossover compared with the internal DX tile helical domains may offer an energetically beneficial location for hydrophobic dyes and dimers.

In the cases discussed above with multiple dyes templated to a single strand, dye-dye interactions—although important for aggregate behavior—are not expected to drive tile formation during annealing because only one strand is templated with dyes; hybridization is typically expected to proceed relatively unaffected by inter-dye attractive forces. In contrast, in this section the following dimer designs include dyes templated to two complementary strands within the DX tile (Fig. 9a). We found that templating dyes to complementary strands can have profound effects on the final system configuration, including the final DNA structure, owing to additional inter-dye attractive forces that can be on the order of base-pair hybridization energy.<sup>62</sup> Moreover, we suggest that the system configuration ultimately results from dyes directly participating with the DNA in a cooperative manner to determine the final configuration and properties of the combined system. These results have significant implications for developing and modeling of reliable, modular, homogeneous, higher-order DNA-dye networks for use as building blocks for next generation aggregate systems.

**3.3.1. Steady-state absorption and PAGE.** In the previous sections, PAGE was used to evaluate the degree of structural



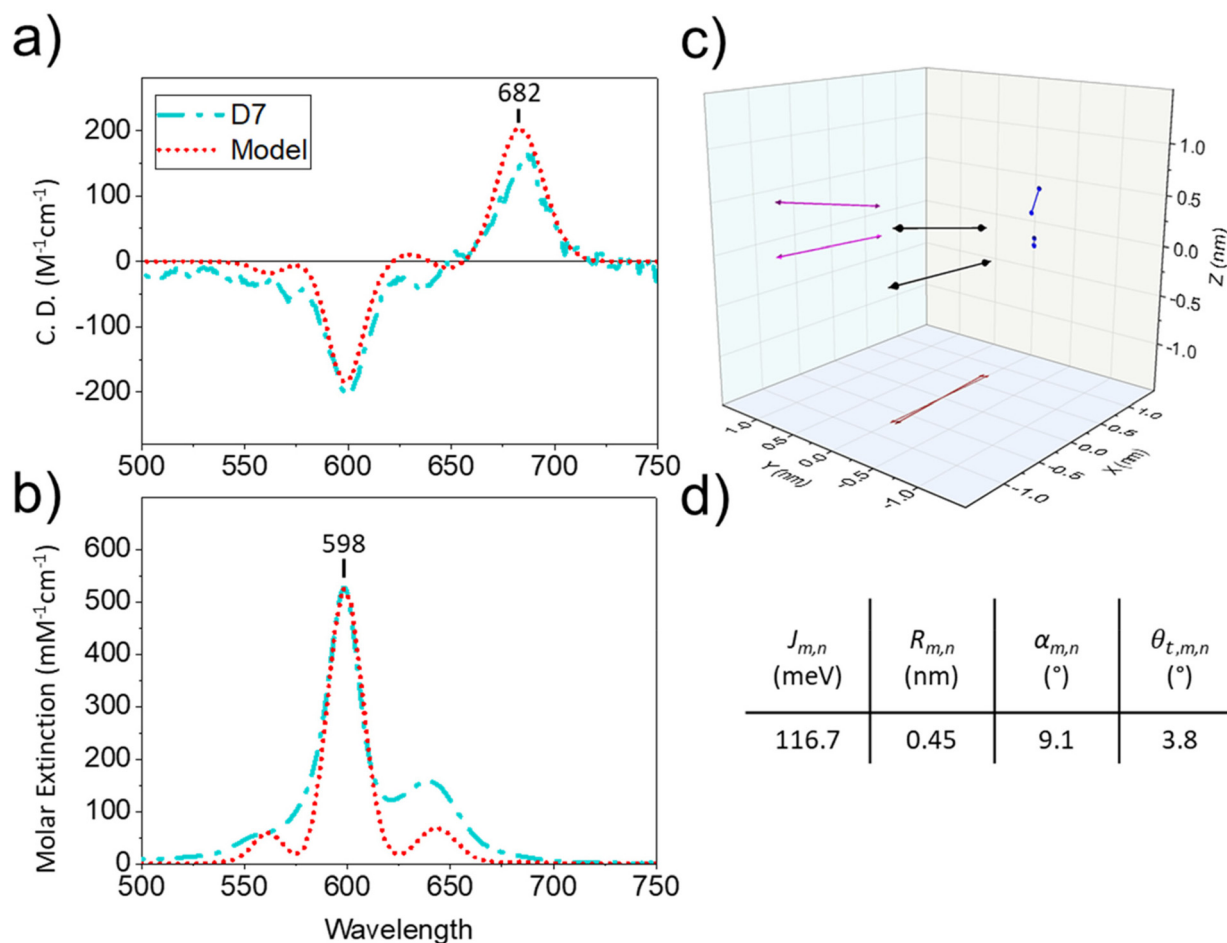


**Fig. 8** Panels (a) and (b) show experimental data (cyan dash-dot; note: 10% native PAGE purified) and KRM-modeled (red dot) CD and molar absorption spectra, respectively, for D7. (c) KRM-derived orientations of TDMs giving rise to the modeled spectra. (d) Summary of key KRM outputs, including  $J_{m,n}$  (excitonic hopping parameter),  $R_{m,n}$  (center-to-center TDM separation),  $\alpha_{m,n}$  (angle between TDM vectors in three dimensions), and  $\theta_{t,m,n}$  (out-of-plane twist). See ESI section S5† for full KRM results and goodness of fit metrics. See also section S12† for additional information regarding uncertainty quantification for KRM modeling.

(DNA) heterogeneity in each sample (see ESI section S2† for gel images). To summarize, constructs with dyes attached to a single strand within the tile generally showed a single prominent gel band with similar gel mobility as an unlabeled DX tile sample. In contrast to the dimer designs presented thus far, PAGE analysis of dimer constructs with dyes templated to opposing strands revealed the presence of multiple prominent gel bands, each with different gel mobility, revealing the heterogeneous nature of the samples in terms of DNA structure. Fig. 9b compares gel mobility for DX tile samples templated with 0–4 dyes. Gel bands with mobility similar to the unlabeled DX tile (bottom row) were assumed to be fully assembled (single) DX tiles. Absorption spectra from these single-tile bands are presented in Fig. 9d. Table 4 provides maximum absorption wavelength and 0–1/0–0 ratios for select extracted gel bands. Notably, gel lanes containing monomer sample **M8** and dimer sample **D7** discussed previously did not show observable gel bands with lower mobility that would indicate higher order or misfolded DNA configurations.

**Table 4** Absorption maxima of select PAGE-purified aggregates and estimated ratios of intensity between the primary aggregate absorption feature (peak 1) and the feature near the monomer wavelength (peak 2)

Construct	$\lambda_{\text{max}}$ Abs. [nm]	Peak 1/peak 2 ratio
<b>DT3</b>	598	4 <sup>a</sup>
<b>D17</b> <sub>lower</sub>	597	1.39
<b>DT1</b>	573	4.57
<b>D18</b> <sub>lower</sub>	593	1.61
<b>DT2</b>	573	5.64
<b>Tet1</b> <sub>lower</sub>	643	0.63
<b>Tet1</b> <sub>upper</sub>	560	3 <sup>a</sup>

<sup>a</sup> Estimated due to low signal-to-noise.

Absorption spectra for monomer **M8**, dimer **D7**, and the higher-mobility gel band of monomer **M6** confirm previously presented spectra and are included in Fig. 9d for comparison. The lower bands of dimers **D17** and **D18** showed signs of H-like aggregation similar to previous dimers (Fig. 9d);



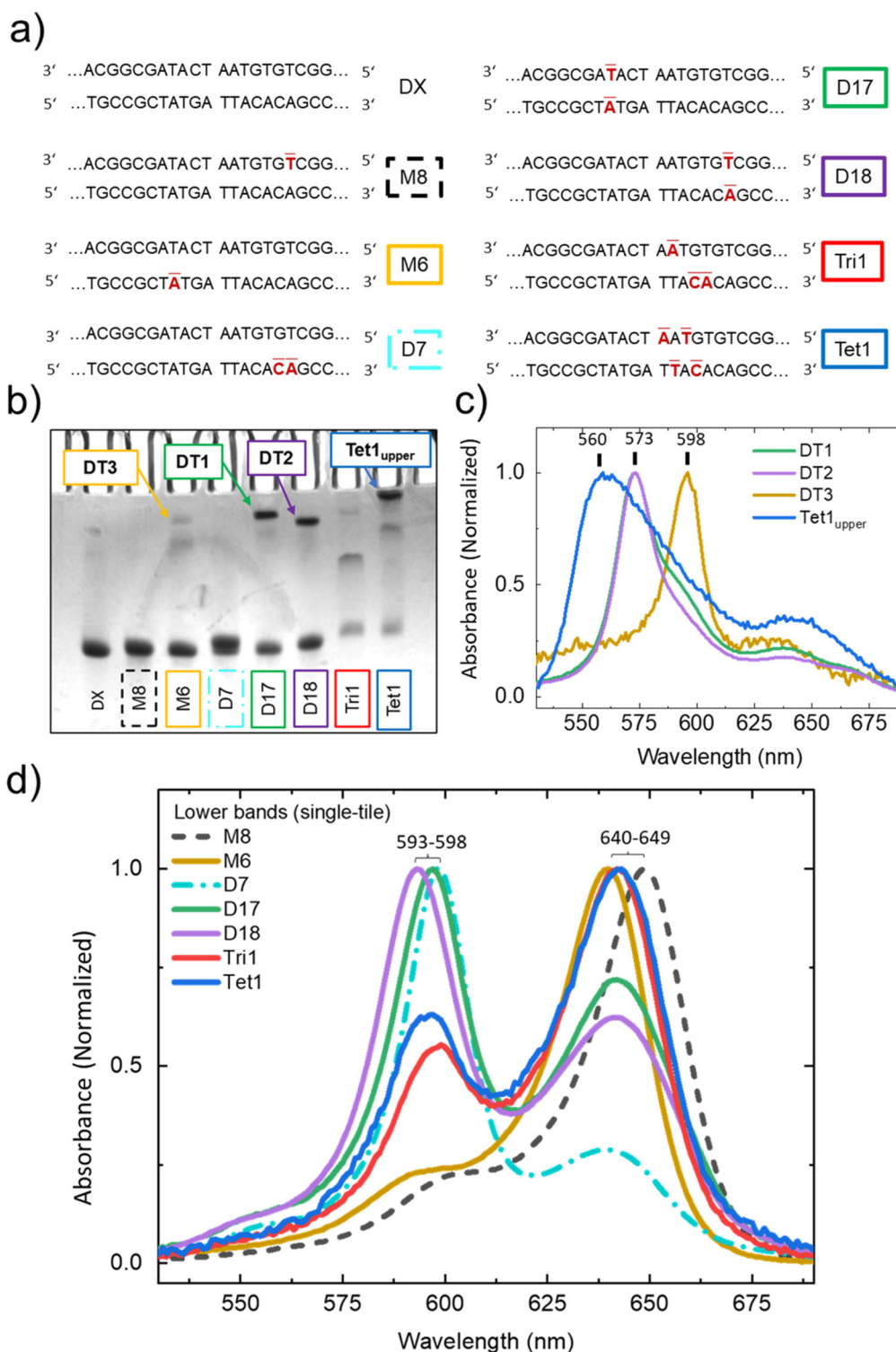


**Fig. 9** (a) Sequences detailing locations of dye-modified bases for an unmodified DX tile and select samples of interest. Dye-modified bases are marked in red with an overbar. Sample names are outlined with colors corresponding to later plots. (b) PAGE gel image of select samples. (c) Normalized absorption spectra of select low-mobility (upper) gel bands labeled in panel b. (d) Normalized absorption spectra of samples extracted from the lower row of bands in panel b. All samples were prepared in 1x TBE, 15 mM MgCl<sub>2</sub>; 10% native PAGE purified (see ESI section S2† for gel images).



however, both constructs also showed significant absorption near the 0–0 monomer transition wavelengths, suggesting decreased coupling and/or significant aggregate subpopulations compared with dimer **D7**. The single-tile gel band for constructs **Tri1** (three dyes) and **Tet1** (four dyes) were relatively faint, suggesting that the majority of the sample material was contained in the lower-mobility bands.

Notably, gel lanes for samples **D17** and **D18**—along with **Tet1** and to a lesser extent, monomer **M6**—contained distinct bands at a much lower mobility than the single-tile constructs. These lower mobility bands were extracted from the gel, with their absorption spectra presented in Fig. 9c (see also Table 4). We note we also observed a gel band for construct **Tri1** with intermediate mobility; however, we defer to ESI section S8† for a discussion related to the relevance of this band to the following results. Aggregate **DT3** (**DT** = “double tile”; see following sections)—the lower-mobility gel band for construct **M6**—was faint; however, the extracted spectrum clearly reflects that of a strongly coupled H-like dimer. The lower-mobility bands for

dimers **D17** and **D18**—denoted **DT1** and **DT2**, respectively—showed an additional hypsochromic (blue) shift from the monomer not observed for any dimer, indicating that additional dyes beyond a dimer were interacting within the aggregate. Furthermore, the extracted spectra of **DT1** and **DT2** strongly resembled previously reported four-dye (tetramer) aggregates of **Cy5**<sup>33,81</sup> and **SQ-Cl<sub>2</sub>**.<sup>42</sup> The upper band for aggregate **Tet1<sub>upper</sub>** had the lowest gel mobility—although the band did move through the gel—and exhibited the most shifted spectrum relative to the monomeric dye. The **Tet1<sub>upper</sub>** spectrum was also significantly shifted from **DT1** and **DT2**, suggesting the possibility that additional dyes (beyond four) were participating in the resulting aggregate.<sup>86</sup>

**3.3.2. Evidence and model for a novel double-tile construct.** Taken together, the significant decrease in gel mobility, combined with the observation of spectra resembling that of constructs with twice the number of dyes as the constituent single-tile monomers, dimers, and tetramers, suggested that the lower-mobility gel bands in Fig. 9b corresponded to con-

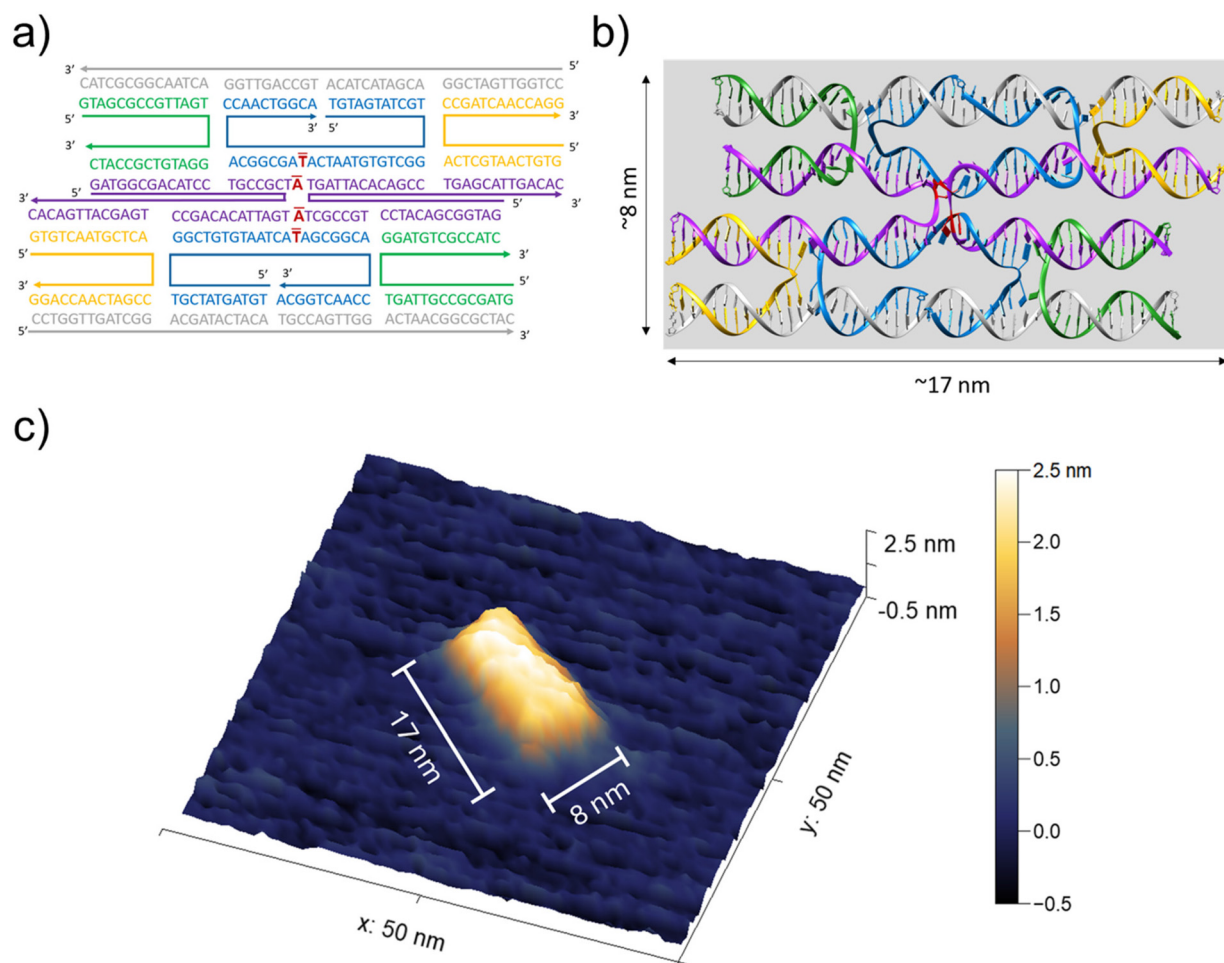


**Fig. 10** (a) DNA sequences, (b) DNA model, and (c) 3D AFM image with z-scale color bar of the proposed novel construct **DT1** forming a double-DX tile, four-dye construct. See ESI section S9† for additional AFM data and measurement profiles. We note that the lateral dimensions indicated refer to the FWHM (full width at half maximum height), rounded to the nearest nm based on the resolution afforded by the 1 nm probe radius and AFM instrument calibration accuracy.



constructs that have combined to form a higher-order DNA construct containing two complete DX tiles. We hypothesize that the components equivalent to the composition of two identical DX tiles (templated with one or two dyes each) combined during the annealing process to form a novel construct. We refer to these as double-tile (DT) constructs. These constructs, as exemplified by **DT1**, formed a new, dye-driven crossover with the branch point at the site of the dye-modified bases on the tile (Fig. 10a and b).

The following sections provide additional evidence to support our hypothesis that the constructs are not simply comprised of two DX tiles that combined, but rather the double-tile self-assembled *de novo* in a cooperative manner in which both the DNA and dyes participated. The findings presented below have profound implications for developing guidelines for designing more complex arrangements of dyes and dye aggregates using DX tile building blocks and singly linked dyes.

First, we rationalized that the observed absorption spectra for **DT1** and **DT2** (Fig. 9c) supported that the lower mobility gel bands contained double-tile, four-dye constructs. The observed spectra were typical of four-dye aggregates previously

reported for Cy5 and **SQ-Cl<sub>2</sub>** in that the absorption maxima were blue-shifted beyond that of any observed dimer of the same dyes. Additionally, relatively little absorption was present at the expected dimer absorption maximum (~600 nm). Thus, we surmised that the observed spectra resulted from an aggregate with more than two coupled dyes. Furthermore, the lack of absorption at the 0-0 monomer transition wavelengths indicated that the samples were free from excessive monomer contamination, which further suggested that the dyes were present in pairs or combinations of pairs. Taken in context with the DNA design, we concluded that the **DT1** and **DT2** constructs contained at least four dyes, and that it was unlikely that the constructs contained more than four dyes, which would require association with additional tiles or excess dye-labeled strands that would be expected to impart an additional blueshift to the absorption maximum.

To further support the four-dye, double-tile hypothesis, we performed KRM modeling of the tetramer constructs to gain further insight into aggregate geometry and coupling. Owing to the additional degrees of freedom in our model imparted by adding dyes beyond a dimer, we were able to model the spectra with multiple similar but distinct configurations of

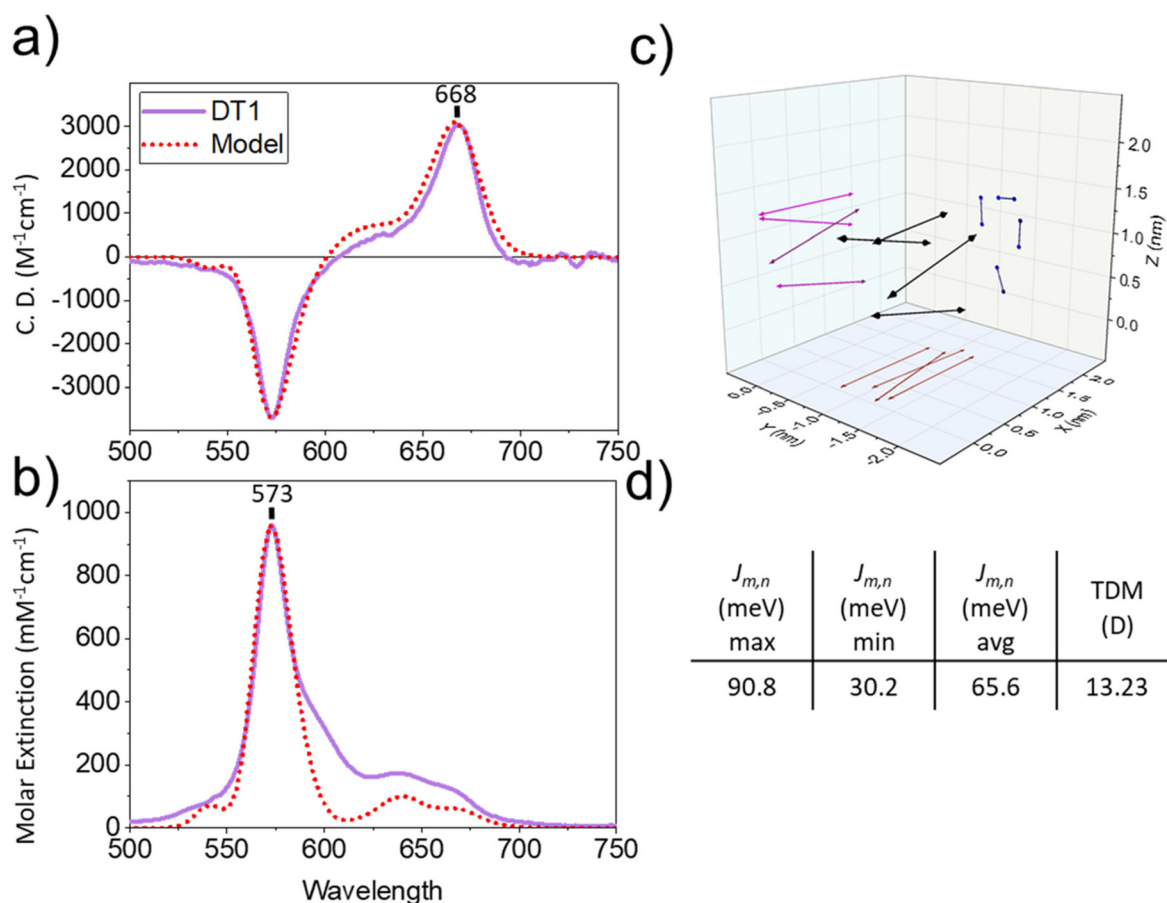


**Fig. 11** Panels (a) and (b) show experimental data (cyan dash-dot; note: 10% native PAGE purified) and KRM-modeled (red dot) CD and molar absorption spectra, respectively, for sample **DT1**. (c) KRM-derived orientations of TDMs giving rise to the modeled spectra. (d) Summary of key KRM outputs. See ESI section S5† for full KRM results and goodness of fit metrics.



TDMs (*i.e.*, the fits are non-unique). In Fig. 11, we present results for one such model (see ESI section S5† for other examples). In this model, the TDMs appeared in a cluster with each TDM coupled to all other TDMs with at least 30 meV of dipole–dipole coupling, a maximum of 90.8 meV between any individual pair of TDMs, and an average of 65.6 meV across all six pairwise interactions. In addition to reproducing the experimental spectral features, we suggest that this was a reasonable model because (1) we expected some steric interference from the dyes and DNA preventing perfect, crystal-like stacking of the dyes, (2) the maximum coupling between any two dyes was comparable to the strongest-coupled dimers of these dyes, and, (3) all dyes being coupled (*i.e.*, no uncoupled, monomer-like TDMs) was consistent with our observation that the samples had very little measurable fluorescence (ESI section S4†). Although the model was able to reproduce the experimental spectra from multiple (similar) arrangements of TDMs (ESI section S5†), the ability of the model to effectively reproduce the observed spectra with a single population of tetra-

mers provided additional evidence that the double-tile constructs contain tetramers that are largely homogeneous in terms of aggregate behavior.

Next, we performed atomic force microscopy (AFM) in fluid (*i.e.*, buffer solution with added salt to encourage surface immobilization of DNA constructs) to confirm that the samples contained DNA constructs of the expected dimensions ( $\sim 17 \text{ nm} \times 8 \text{ nm}$ ; Fig. 10b) for the double-tile case (expected dimensions of a single tile are roughly  $15 \text{ nm} \times 4 \text{ nm}$ ). Although the precise conformation of the double-tile construct in solution is unknown, one expects that double-tile constructs that adhere to the mica substrate used in AFM would adopt an “open” configuration to maximize interactions between the negatively charged DNA backbone and the divalent cation-treated mica surface. Despite the challenges associated with imaging DNA constructs of this size, AFM indicated the presence of constructs of the expected size for our double-tile model as depicted in Fig. 10c and d. See ESI section S9† for additional details regarding AFM results and protocol.

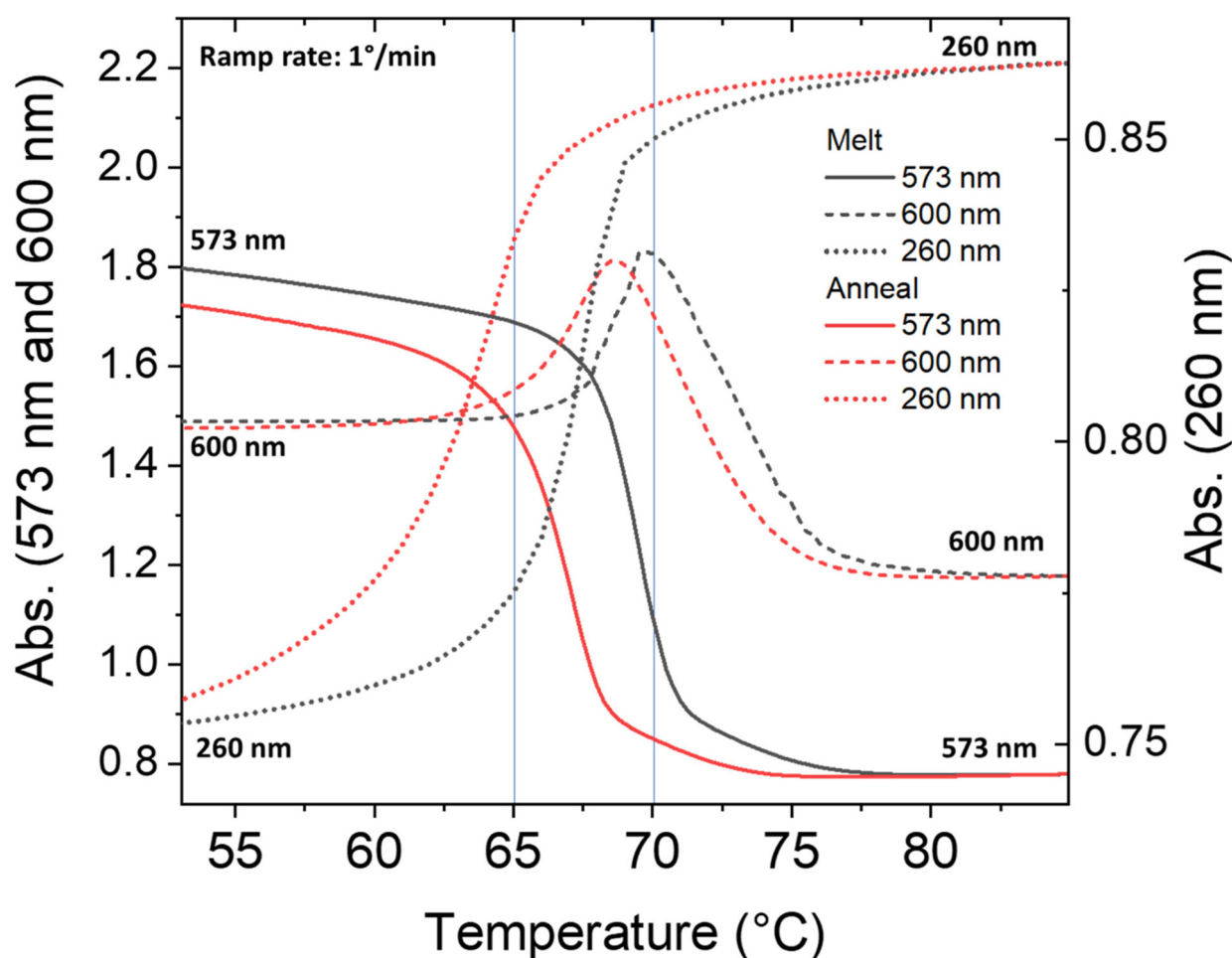


**Fig. 12** Wavelength-dependent melting and annealing profiles (absorbance as a function of temperature at specified wavelengths) for DT2 during a  $1^\circ \text{ min}^{-1}$  temperature ramp while melting from 25 °C to 95 °C (black traces) and annealing from 95 °C back to 25 °C (red traces). The vertical lines define temperatures representing points in the annealing process at which specific dye aggregates appear to be preferentially formed. These points provided guidance to further explore optimal annealing schedules.



To further explore the manner in which the double-tile constructs assemble, we performed DNA melting and annealing experiments while monitoring absorption at multiple wavelengths. Fig. 12 shows melting and annealing profiles for a high-concentration sample of **D18** at the DNA absorption feature (260 nm), approximate dimer maxima (600 nm), and observed four-dye (tetramer) maximum (573 nm). A high concentration was selected for this experiment to ensure that a significant population of double-tile constructs was present in the sample (see section 3.3.3 and Fig. 13).

The melting (annealing) profiles suggested that the samples dissociated (associated) in a multi-step process as temperature increased (decreased). We estimated that the DNA melting point occurred at roughly 67 °C (ESI section S7†), whereas the tetramer absorption was largely unchanged at 68 °C and the absorption at the dimer feature increased

slightly. These observations suggested that the double-tile constructs initially dissociated into two mostly complete single-tile constructs—decreasing the number of tetramers and increasing the number of dimers present in the solution. As the temperature increased to 70 °C, the tetramer absorption decreased sharply and the dimer absorption increased, indicating a conversion from four-dye aggregates to two-dye aggregates. Above 70 °C, the tetramer population was depleted, and the dimers continued to dissociate until approximately 80 °C, at which point the sample had completely dissociated into its single-strand components.

The annealing profiles reflected assembly in reverse order, as expected, and each wavelength showed different degrees of hysteresis. The 600 nm profile suggested that monomers combined to form dimers as temperature decreased from 75 °C to 68 °C. Then the dimers began to combine into tetramers, indi-

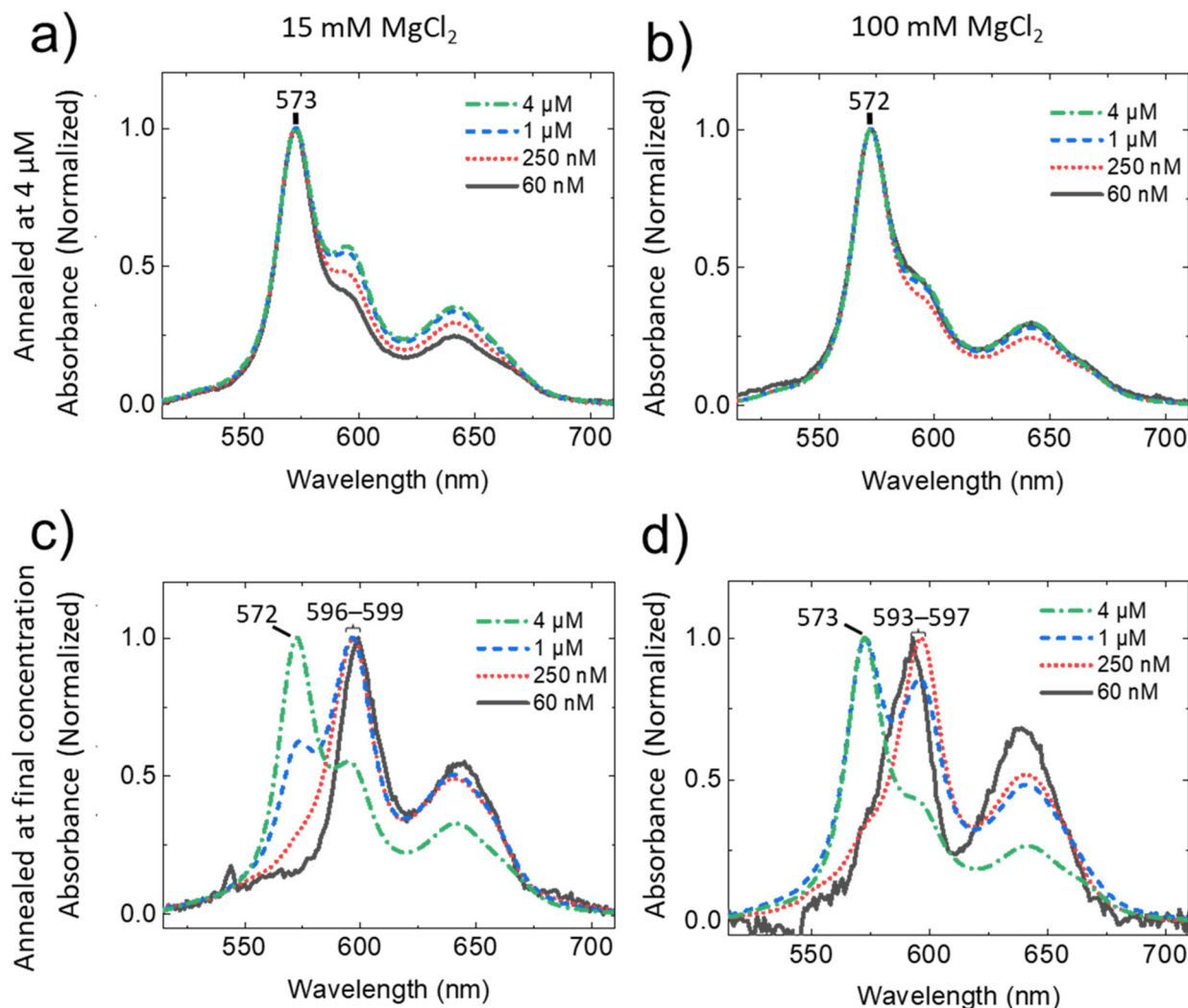
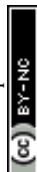


**Fig. 13** Normalized absorption spectra of (unpurified) **D17** prepared at 4  $\mu\text{M}$  with either 15 or 100 mM  $\text{MgCl}_2$ . Each sample was divided in half and then each half was subjected to different annealing and dilution (to modulate DNA concentration) protocols as follows: (a) 15 mM  $\text{MgCl}_2$  annealed at 4  $\mu\text{M}$  and then diluted to final concentration. (b) 100 mM  $\text{MgCl}_2$  annealed at 4  $\mu\text{M}$  and then diluted to final concentration. (c) 15 mM  $\text{MgCl}_2$  diluted to final concentration and then annealed. (d) 100 mM  $\text{MgCl}_2$  diluted to final concentration and then annealed. All samples annealed at 95 °C for 5 minutes and cooled at 0.4 °C  $\text{min}^{-1}$  until 25 °C.



cated by the steep rise in the absorption at 573 nm and concurrent decrease in dimer absorption. Finally, the DNA associated—indicated by the reduction in absorption at 260 nm—at an annealing temperature of approximately 63 °C (see ESI section S7† for unlabeled tile melting/annealing data). We note that the tetramer aggregates appeared to be nearly completely assembled even while the DNA was still partially dissociated. The annealing results indicated that (1) the dyes aggregated before the DNA, suggesting a cooperative assembly initiated by dye–dye interactions, (2) the DNA–dye aggregates formed directly during annealing as opposed to relying on a DNA branch-migration process after the tiles were fully formed, and (3) the aggregation process was self-limiting. Apparently, additional dye-labeled DNA strands were not able to participate once a tetramer was formed and the DNA partially hybridized adjacent to the dye attachment points. Absorption spectra collected during melting/annealing cycles confirmed that the double-tile constructs were robust up to temperatures near the DNA melting temperature (ESI section S7†).

**3.3.3. Additional characterization and controlled assembly of double-tile constructs.** To further investigate the conditions that affected the formation of double-tile constructs and to gain control of assembly of resulting samples and their properties, we produced a series of samples with differing DNA concentrations,  $\text{Mg}^{2+}$  concentration in the buffer solution, and annealing treatments (Fig. 13). We chose **D17/DT1** (Fig. 9) to represent the double-tile constructs. To begin, two samples with large solution volumes were prepared at high (4  $\mu\text{M}$ ) concentration with either 15 mM or 100 mM added  $\text{Mg}^{2+}$ . Each sample was annealed at 95 °C and its absorption spectrum was recorded at 22 °C. A portion of each sample was separated and diluted with additional buffer to span roughly two orders of magnitude in DNA concentration. Absorption spectra were

collected (at 22 °C) for each sample both without additional annealing (Fig. 13a and b) and after annealing at the final concentration (Fig. 13c and d). All samples that were annealed at 4  $\mu\text{M}$  showed absorption spectra comparable to the gel-purified tetramers (**DT1** and **DT2**; Fig. 9c). Although the 15 mM  $\text{Mg}^{2+}$  sample set showed small differences in spectra after diluting the sample, the spectra were largely unchanged and indicated that the observed tetramer spectra were robust and insensitive to  $\text{Mg}^{2+}$  concentration or changes in DNA concentration after annealing. In stark contrast, the samples that were annealed at their final concentration showed distinct changes in their spectra as concentration decreased. Fig. 13c and d clearly show that the sample constituents strongly depended on the DNA concentration during the annealing step, with a weaker but still significant dependence on  $\text{Mg}^{2+}$  concentration. Each dilution step decreased the relative proportion of tetramers compared with dimers until 250 nM; in contrast, the 60 nM spectra largely reflected the 250 nM spectra (Fig. 13c and d). These results also confirmed the discrete nature of the conversion from two-dye (600 nm absorption maximum) to four-dye (573 nm absorption maximum) aggregates, rather than a continuous change in the peak position.

The preceding experiments were performed using a fixed annealing cycle with a ramp rate of 0.4 °C  $\text{min}^{-1}$ . To further refine the sample preparation protocol, we used previous melting and annealing data to inform more complex annealing schedules. A 5  $\mu\text{M}$  sample of **D18** was heated to 95 °C and held for 5 minutes to completely dissociate the DNA into single strands. The sample was then subjected to each of the annealing schedules depicted in Fig. 14a, with the resulting absorption spectra shown in Fig. 14b. Quickly driving the sample temperature to room temperature (“Crash” in legend of Fig. 14a) resulted in a spectrum that was dominated by

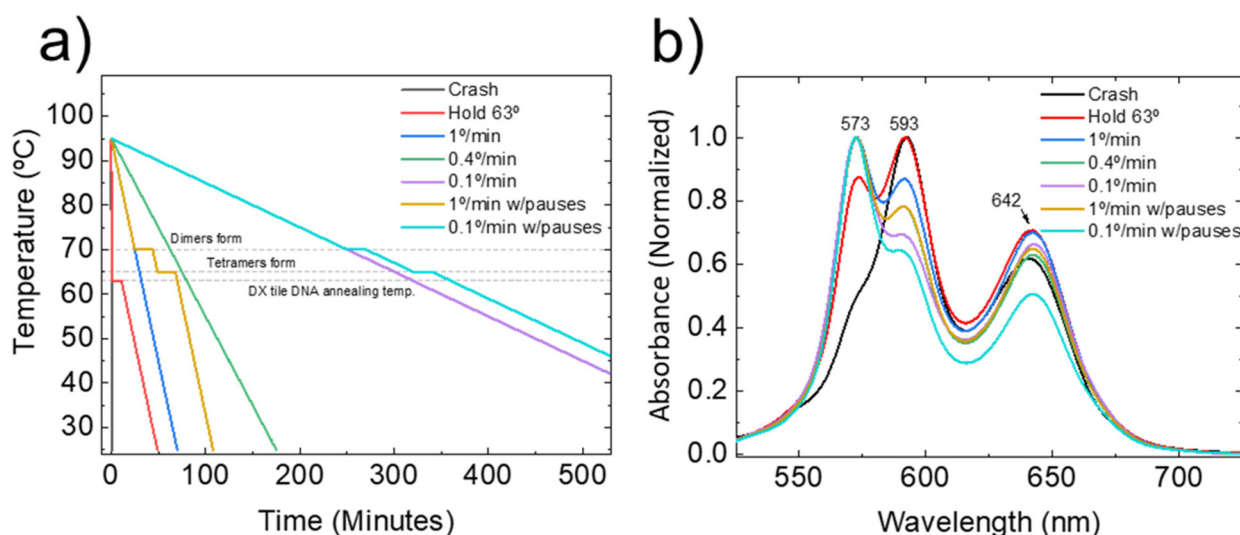


**Fig. 14** (a) Annealing schedules with indicated regions of subpopulation formation and (b) corresponding absorption spectra for a suite of annealing treatments. Horizontal lines in panel (a) correspond to the temperatures highlighted in Fig. 12 and the annealing temperature of the unlabeled DNA template (ESI section S7†).



absorption near 600 nm, as expected for (dye) dimers with relatively little tetramer absorption. Driving the sample to the unlabeled DX tile annealing temperature of 63 °C (*i.e.*, annealing the tile as though no dyes were present and minimizing opportunities for dye–dye interactions to affect assembly) and holding it for 10 minutes before cooling to room temperature at 1 °C min<sup>−1</sup> resulted in a heterogeneous sample with distinct absorption peaks corresponding to dimers and tetramers. A continuous (annealing) ramp rate of 1 °C min<sup>−1</sup> further increased the proportion of tetramers in the sample. Additionally, the proportion of tetramers in the sample was further enhanced by holding the sample at temperatures informed by the data in Fig. 12. That is, the sample was held at 70 °C for 20 minutes to promote the formation of dye dimers, and then the sample was held at 65 °C for 20 minutes to promote the formation of dye tetramers before cooling to room temperature (Fig. 14a, gold trace). The resulting absorption spectrum was nearly identical to the spectrum obtained when the sample was cooled at a rate of 0.4 °C min<sup>−1</sup> (Fig. 14b, gold and green traces) with a 37% reduction in overall annealing time. Extended annealing cycles with ramp rates of 0.1 °C min<sup>−1</sup>, both without and with the aforementioned pauses, resulted in further increases in tetramer absorption relative to dimer absorption. These results suggested that annealing schedules can be optimized to tune sample properties, reduce both DNA and aggregate heterogeneity, and increase the yield of desired constructs. Although the specific conditions necessary to optimize a given system will depend on many factors, we suggest that a combination of wavelength-dependent melting profiles, salt and sample concentrations, and controlled annealing schedules can provide a blueprint that enables optimization of systems composed of multiple components that each participate in the self-assembly process.

**3.3.4. Transient absorption experiments.** To characterize the excited-state lifetimes of the dimer **D7** and tetramer constructs, **DT1** and **DT2**, we performed TA experiments. Each sample was excited at its absorption maximum. Samples were analyzed with a white-light probe. Fig. 15 shows the resulting surface plots (top row), spectra at selected time delays (middle row), and kinetics at select wavelengths (bottom row).

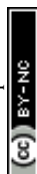
Dimer **D7** showed a ground-state bleach (GSB) feature that generally reflected its absorption spectrum. We noted the presence of a small amount of monomer contamination arising from incomplete purification in this sample that resulted in a small amount of fluorescence. The presence of a small monomer population was confirmed with global target analysis (GTA; ESI section S10†) by including a parallel decay of a monomer component with a fixed lifetime of 3 ns. Apart from the residual monomer contamination, TA and GTA results—taken in context with our other findings—supported the finding that the **D7** sample was largely homogeneous. The **D7** dimer kinetics were fit with a two-step sequential decay including an initial fast (600 fs) relaxation followed by a much slower decay to the ground state. The **D7** dimer showed a significant reduction in its population lifetime from the monomeric form

of the dye with an excited-state lifetime of 37.4 ps. We did not observe spectral features indicative of the charge-transfer state recently reported for another DNA-templated double linker squaraine dimer.<sup>62</sup> Similarly, tetramer samples **DT1** and **DT2** showed a dominant GSB feature at 570 nm corresponding to their UV-Vis absorption maximum. Tetramer kinetics were again fit using a two-step sequential decay with a fast relaxation (400 fs) followed by decay to the ground state. Remarkably, the excited-state lifetimes of the tetramer samples—even though they are templated to different parts of the tile—were nearly identical (61.3 ps *vs.* 64.1 ps) and, furthermore—and of interest—both tetramer lifetimes were nearly double that of the **D7** dimer. We note that a monomer component was not required to sufficiently describe the tetramer TA data using GTA. Taken in context with other results, these data suggested that the tetramer samples were largely homogeneous in terms of dye-aggregate behavior, at least with respect to their photo-selection by pumping at their absorption maxima.

**3.3.5. Transfer to solid phase.** Fig. 13 implied that—once formed during annealing—double-tile tetramer constructs had spectra that were largely robust to changes in DNA or Mg<sup>2+</sup> concentration. It is of theoretical and technological interest to explore the robustness of DNA–dye constructs and their spectra when transferred to other environments, in particular, when adsorbed onto a surface and dried (*i.e.*, solid phase). To explore the behavior of the DNA–dye systems when immobilized on a surface and removed from an aqueous solvent, a selection of samples was transferred to glass slides and allowed to dry undisturbed at room temperature. The absorption spectrum of each dried sample was then collected by placing the dry sample in the beam path of UV-Vis and CD spectrometers.

For context, we return first to the monomer samples. Monomer sample **M8**—in agreement with Fig. 5 that provided evidence for intercalation—showed no change in absorbance when transferred from solution to solid phase (Fig. 5d and 16a), suggesting that the dye was protected from the more polar solvent by the surrounding DNA environment. Monomers **M6** and **M7**, however, showed slight red-shifts in their absorption maxima, and, notably, all three monomers had an absorption maximum at 649 nm when dried on the glass slide. The latter result further suggested that differing degrees of exposure to the solvent and DNA (that is, the polarizability of the surrounding environment) were responsible for any differences in absorption maxima observed in aqueous *versus* dried monomer samples.

Two other attributes of sample **M6** were of note. First, a higher concentration (4 μM) sample in solution—when considered in the context of the double-tile model presented above and the gel band observed in Fig. 9b—appeared to be susceptible to forming double-tile (dye) dimers, with an absorption peak appearing at ~600 nm in accordance with other dimer spectra. Although we were able to extract and characterize the double-tile band from **M6**, the yield was relatively low, with the majority of the sample material contributing to the single-tile construct. Second, upon drying, sample



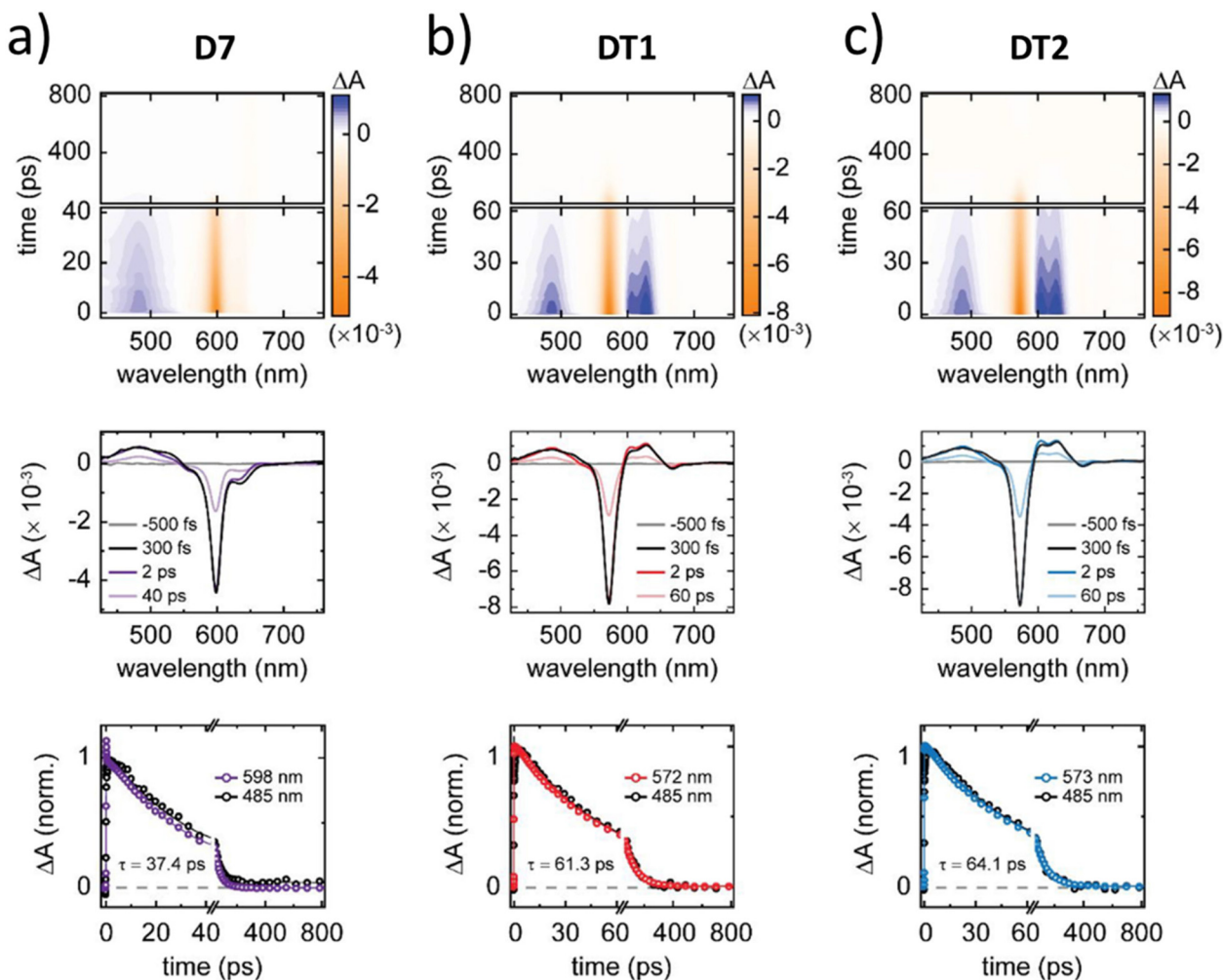


**Fig. 15** Femtosecond TA of (a) D7, (b) DT1, and (c) DT2. The top, middle, and bottom rows display TA surface plots, selected kinetics, and selected spectra, respectively. The pump wavelength for D7 was 600 nm, whereas the pump wavelength for DT1 and DT2 was 570 nm. In all measurements, a pulse energy of  $\sim 14$  nJ was used and the pump spot size was determined to be  $\sim 170$   $\mu\text{m}$ , yielding an energy density of  $\sim 60$   $\mu\text{J cm}^{-2}$ . Dimer and tetramer lifetimes obtained from a GTA of the data are displayed in the bottom panels. In the bottom panels, circles and lines represent the data and fit, respectively. Additional details on the GTA, including the kinetic scheme used to model the data, are provided in section S10.† All samples were prepared in 1x TBE, 15 mM  $\text{MgCl}_2$ ; 10% native PAGE purified.

**M6** also showed an enhanced peak near 600 nm in solid phase that suggested formation of additional dimers upon adsorption. We suggest that the additional dimers arose from monomeric dyes that had settled onto the exterior of the tile, which then enabled the dyes to dimerize when dried into a film. An alternative explanation for additional dimerization in solid phase could be that two separate tiles combine *via* a branch migration process<sup>87</sup> during the drying process as the  $\text{Mg}^{2+}$  concentrations become extremely high; however, our observations could not distinguish between either possibility. We note that both of the observed absorption peaks in the solid phase **M6** sample were red-shifted relative to the corresponding solution sample, which supported the finding that the peak shifts arose from changes in environment polarity and polarizability.

Absorption spectra for dimer **D7** showed a similar red-shift in peak position (6 nm or  $\sim 20$  meV) upon transfer to solid

phase (Fig. 16b), suggesting that dimer **D7** was at least partially exposed to a more polar environment (*e.g.*, more exposure to aqueous buffer) in solution or that the dimer packing geometry or interactions with the DNA were altered slightly upon drying. Although a small increase in absorption at longer wavelengths ( $\sim 650$  nm) was observed, we did not observe additional absorption features at wavelengths shorter than 598 nm. The lack of additional absorption features suggested that the dimers were sufficiently isolated by the DX tile such that the dimers did not couple to other nearby dyes when transferred to solid phase. We note that the **D7** dimer sample did not show an observable CD spectrum in solution or solid phase, suggesting that the dimer maintained its planar arrangement when transferred to solid phase. Overall, the spectra indicated that the dimer remained largely unchanged and maintained the strong coupling and exciton delocalization observed in solution when transferred to solid phase.



Tetramers arising from dimer designs **D17** and **D18** were prepared at high concentrations (8  $\mu\text{M}$ ) to maximize the ratio of tetramers to dimers in accordance with results from Fig. 13. Solution spectra confirmed that the absorption spectra were dominated by a peak at  $\sim 573$  nm as expected for **SQ-Cl<sub>2</sub>** tetramers (Fig. 16c and d). Each solution sample showed CD features corresponding to the allowed absorption maximum and the optically suppressed (due to symmetry) lower exciton state

at  $\sim 667$  nm. In solid phase, both samples showed a small shift in absorption maxima ( $\sim 30$  meV). Interestingly, the lower exciton state—marked by the lower-energy CD feature—showed a significantly smaller red-shift of  $\sim 5$  meV. We attribute these changes to a combination of possible slight changes in aggregate packing and changes in environment polarizability and polarity. As with dimer **D7**, the double-tile tetramers appeared to maintain their spectral properties when

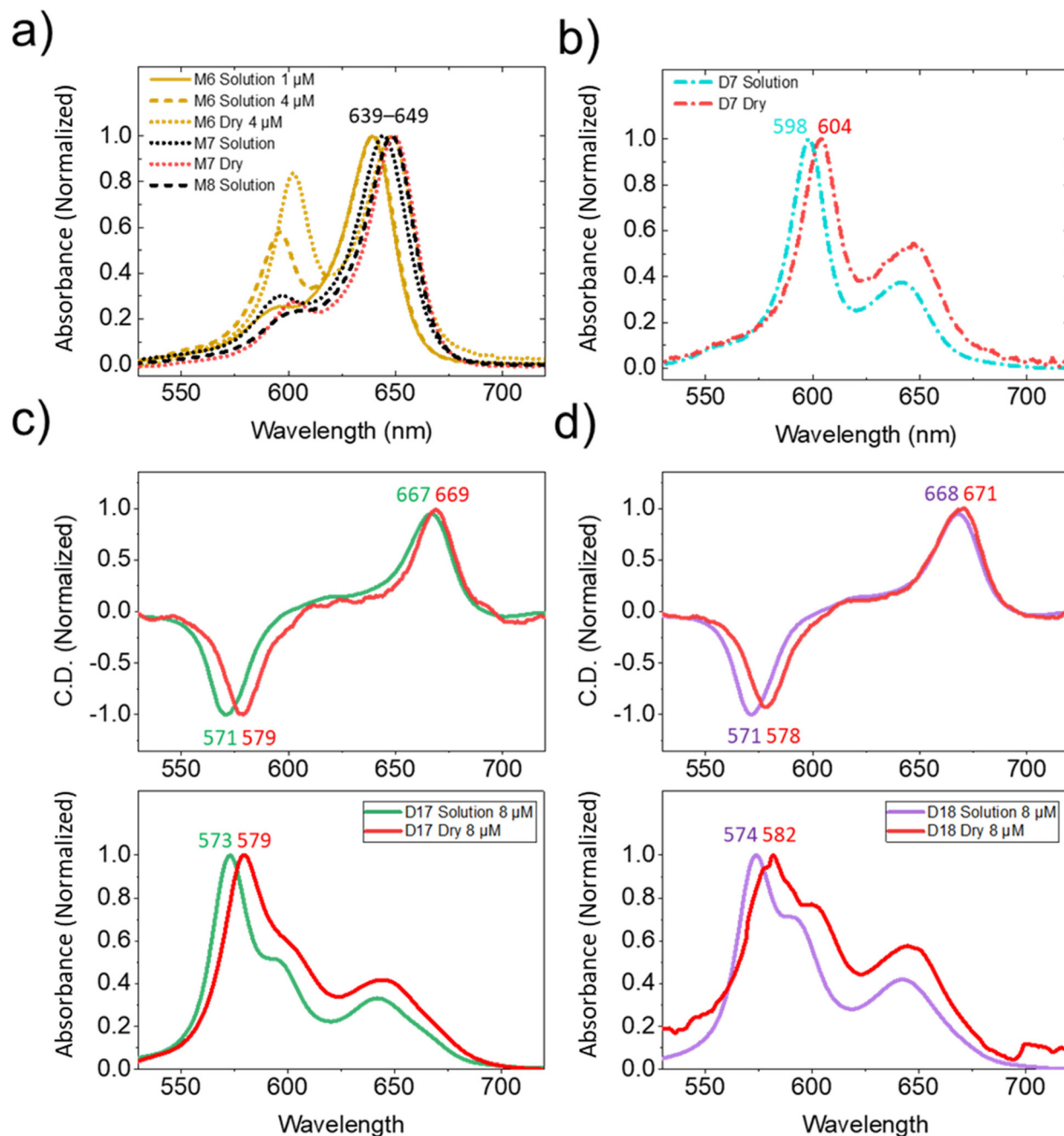


**Fig. 16** (a) Normalized absorption spectra of monomer samples **M6** and **M7** in solution versus dried with sample **M8** in solution plotted for comparison. (b) Normalized absorption spectra of sample **D7** in solution versus dried. (c) Normalized absorption (bottom) and CD spectra (top) of sample **D17**. (d) Normalized absorption (bottom) and CD spectra (top) of sample **D18**. All solution samples were prepared in 1x TBE, 15 mM  $\text{MgCl}_2$ . Images of solid-phase samples are provided in ESI section S11.†



transferred to solid phase, indicating that the aggregates maintained the strong exciton delocalization observed in solution despite any minor conformational changes that may have occurred in the DNA. The similarity in CD spectra between solution and solid phases further demonstrated that the aggregates maintained similar configurations in both environments. Similar to **D7**, we did not observe evidence of secondary coupling between tetramers in solid phase, suggesting that the DNA scaffold sufficiently isolated the tetramers from additional aggregation when dried onto the glass surface.

**3.3.6. Discussion.** The previous sections presented a model for controlled self-assembly of strongly coupled squaraine tetramers tethered at the crossover junction that resulted in a doubling of the composition of a single DX-DAE tile to form a double tile (Fig. 10a and b). The tetramers formed at this specific crossover were comparable to previous tetramer aggregates of the same dye (**SQ-Cl<sub>2</sub>**) templated by a HJ;<sup>42</sup> however, their intense and well-defined CD spectra suggested that the double-tile tetramers presented here are well-ordered and more homogeneous, with a preference for a right-handed chiral configuration. This was in contrast to the comparatively muted CD spectrum arising from the HJ-templated tetramer, which may take on multiple DNA conformations (*i.e.*, structural heterogeneity) potentially leading to different dye orientations that were likely either achiral (*i.e.*, planar TDMs) or were comprised of subpopulations of aggregates with mirror-image geometries leading to a cancelation of the component CD signals.<sup>42</sup>

The double-tile model was supported by multiple methods of physical characterization including UV-Vis, CD, and TA spectroscopy, PAGE, and AFM. Theoretical support *via* KRM modeling demonstrated that the observed spectra could not be reproduced by a two-dye model. Instead, a four-dye model best reproduced the observed spectra, though multiple distinct tetramer configurations were able to similarly and adequately describe the absorption and CD responses (Fig. 11; ESI section S5, Tables S10–S12;† OI<sub>ABS</sub> and OI<sub>CD</sub> > 0.9). In the following paragraphs, we describe the design aspects and sample conditions that influenced the resulting constructs and their properties.

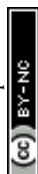
The specific aggregate arrangement on the tile had the most influence on double-tile formation under the studied conditions. In general, tiles with multiple dyes templated to the same strand did not form appreciable quantities of double tiles in PAGE images (ESI section S2†). Furthermore, with the exception of **M6**, tiles with single dyes did not tend to form double-tile constructs. Sample **M6** formed a minor subpopulation of double tiles as evidenced by PAGE imaging and the observation of characteristic H-like dimer absorption from the extracted gel band (Fig. 9). In contrast, gels and spectra indicated that some tiles templated with dyes on opposing strands attached at a single complementary base pair, readily formed both single and double-tile structures. We note that the geometry of the specific base pair in relation to the tile also played a role in double-tile formation. Specifically, the dyes in constructs **DT1** and **DT2** were templated to the tile approximately

*one full turn of the helix apart*, resulting in roughly the same orientation of the modified base pair on the tile. Both constructs exhibited remarkably similar properties, including UV-Vis and CD spectra and excited-state lifetimes. Conversely, a construct with one attachment location offset by a single base compared with **DT1** showed a lower propensity to form double-tile structures (ESI section S2†). We suggest that the geometry of the dye linkers extending from the templated base pair and their attachment location with respect to the helical twist of the DNA were significant factors that influenced the capability of the dyes to direct DNA self-assembly toward forming double-tile structures (see further discussion below).

We note that attempts to template three and four dyes on neighboring base pairs had limited success. In particular, construct **Tri1** formed several bands in the gel (Fig. 9b), indicating the presence of significant structural heterogeneity. We suggest that dye–dye interactions and decreased structural integrity of the tile contributed to the observed gel bands. See ESI section S8† for further analysis of **Tri1**. Construct **Tet1** also produced multiple gel bands (Fig. 9b), with a high-mobility band (**Tet1<sub>lower</sub>**) comparable to other single-tile construct bands and two bands with lower mobility. The slowest band (**Tet1<sub>upper</sub>**) barely moved in the gel; however, its absorption spectra showed the greatest shift from the monomer, suggesting that the upper gel band was likely to contain a double-tile, eight-dye construct. Attempts to reduce sample heterogeneity by increasing Mg<sup>2+</sup> concentration resulted in runaway aggregation and a phase change (ESI section S2†). We suggest that attempts to cluster additional dyes to form larger aggregates on a single tile could be problematic due to excessive dye–dye interactions that preclude reliable formation of intended constructs that remain in solution.

For the samples that formed the double-tile structure, the relative proportions of single- *versus* double-tile constructs in the samples were found to be both structurally and spectrally tunable through careful control of sample conditions during self-assembly. The concentration of the tile components in the sample solution—during annealing—had a profound impact on the sample contents and resulting spectra (Fig. 13). Controlling the concentration of Mg<sup>2+</sup> in the sample solutions during annealing provided an additional means of tuning the solution to select between single and double tiles (and their associated spectra; Fig. 13). Furthermore, adjusting the annealing schedule (Fig. 14) further influenced the sample contents, providing additional tunability to select single- or double-tile constructs. For example, in the case of **D17** and **D18**, we were able to select between formation of either dimer or tetramer aggregates and their respective absorption spectra. Interestingly, pausing briefly at specific points in the annealing schedule during the 1° min<sup>−1</sup> annealing cycle provided a means to promote formation of double tiles while also reducing overall annealing time (and resulting in practically identical spectra) compared with a continuous but slower 0.4° min<sup>−1</sup> annealing ramp rate.

The wavelength-dependent annealing profiles presented in Fig. 12 provide insight into the assembly pathway of the



double-tile constructs. A standard approach to DNA hybridization involves mixing of component strands, which are then heated well above their melting temperature before cooling. As the solution cools, the component strands hybridize at different temperatures based on their composition. In general, longer strands will have higher melting (and annealing) temperatures than shorter strands. Typically, hybridization occurs in three steps. First, complementary strands collide in solution to nucleate a few base pairs. Next, the DNA strands rearrange such that the complementary strands have the correct geometry to hybridize. Finally, the strands “zip” together to form the double-helix. For a successful collision, the final two steps must occur while the components are still in contact from the initial collision. These three steps, however, may be impacted when dyes are labeled to DNA strands due to dye–dye interactions.

In the case of the double-tile constructs, the attached dyes contributed to the assembly path by imparting additional bulk to the strands—increasing the collision cross-section and probability of strands meeting in solution—and by adding additional attraction between the strands through dye–dye interactions. The hydrophobic nature of the dye linkers<sup>42</sup> also may have contributed to inter-strand attraction and resulting hybridization. Fig. 12 indicates that the dyes were able to aggregate before the DNA hybridized as temperature decreased, suggesting that the dyes nucleated an aggregate (initially a dimer) at a higher temperature than the attached DNA strands nucleated a base pair. Furthermore, as temperature decreased, the dimers aggregated with each other to form tetramers, with the majority of dimers converting to tetramers before the DNA significantly hybridized. The assembly of the tetramer aggregate before the DNA components assembled enabled the dyes to assemble into their most energetically favorable arrangement before the DNA assembled. This assembly process represents a departure from conventional dye arrangement strategies that rely solely on the DNA to direct the dyes into a desired configuration. We note, however, that the assembly was not purely dye-driven, but rather a cooperative effort by the dyes and DNA.

## 4. General discussion

In this study, we have demonstrated a prototypical DNA–dye system that incorporated single-linker dyes into modular DNA DX-DAE-tile-based constructs. Intuition may suggest that attachment by a single long flexible linker could be detrimental to achieving reproducible and desirable aggregate arrangements; however, we suggest that the flexibility of a long linker allowed a dye to sample a larger volume of space and more freely associate with nearby dyes such that strongly coupled, homogeneous, robust, and reproducible aggregates were obtained from appropriate arrangements. Furthermore, we suggest that a long linker and strong dye–dye interactions (e.g., *via* hydrophobic, permanent ground-state charge distribution, and van der Waals forces) increased the probability of success-

ful collisions during the hybridization process and provided a degree of temporal control during hybridization *via* a programmed annealing schedule. Such an approach has been previously demonstrated for parallel DX tiles,<sup>48</sup> albeit in the absence of templated dyes.

Although this study was focused on systems with multiple interacting dyes, exploration of the properties of the dye-tile system for single dye attachments is key to understanding more complex arrangements of dyes. The reliable intercalation of the dye in sample **M8** has a few interesting implications. The sample design appears to offer a test bed to characterize the tendency for other planar, hydrophobic, and cationic (or, as demonstrated here, zwitterionic) dyes to intercalate at the crossover junction by adjusting the sterics and electrostatics of their individual structures. Based on results using **SQ-Cl<sub>2</sub>**, intercalation also appears to overcome excited-state quenching and extend the excited-state lifetimes of dyes that are prone to isomerization from single-bond rotation within the conjugated *pi* network. Suppression of this bond rotation could provide a method to increase fluorescence in certain types of dyes. The increased fluorescence and potentially consistent location of the intercalated dye with respect to the tile may provide additional benefits for advanced applications such as single-molecule imaging. Additionally, the intercalated dye could function as a reporter dye in a FRET or exciton-based energy transfer scheme, with potentially broad applications, including QIS.

Constructs templated with two dyes on the same strand revealed a wide range of aggregation properties depending on the location of the attachment on the tile. In many arrangements, the flexibility of the linker and the fortified stability of the central domain of the tile resulted in somewhat unpredictable behavior; however, dimer **D7**—templated nearest to a crossover junction—formed robust and homogeneous aggregates with coupling comparable to the most strongly coupled DNA-templated squaraine dimers reported to date.<sup>42,43,60,62</sup> We suggest that the additional flexibility of the crossover junction compared to the interior helical domain of the tile may have enabled the hydrophobic dyes to aggregate in a more homogeneous manner than dimers that were strictly groove-bound on the exterior of the tile. The templated dimer **D7** provides a test system and a benchmark in terms of coupling strength and homogeneity for comparing aggregation properties of similar single-linked dyes, and the modularity of the DX-tile provides a means to arrange periodic arrays of dimers for exploring advanced dye-aggregate networks.

Templating aggregates larger than a dimer on a single DX tile proved to be challenging. We surmise that the inter-dye attractive forces, combined with any disruption in the DNA structure imparted by dye inclusion compared to un-modified DNA, resulted (in our study) in malformed DNA or runaway aggregation. We suggest, however, for templating aggregates resulting in more than two dyes, larger and more stable DNA constructs would be beneficial. Indeed, our double-tile results demonstrated that a larger scaffold can overcome disruptive dye–dye attractive forces to support a robust four-dye aggregate.



**Table 5** Findings and factors important for developing design guidelines for templating singly linked hydrophobic dyes and aggregates to DX tiles. Note that sections, figures, and tables beginning with "S" refer to information in the ESI†

Finding/factor	Evidence	Implications/impacts
1. Dye attachment location on the tile is important.	Significant variations in optical properties were observed from arrangements of identical dyes that were templated to different parts of the same DX tile.	Choices of dye attachment location and linker designs are critical to dye-DX-tile behavior.
2. Dyes/aggregates at crossover junctions are well-behaved.	Monomers nearest to the crossovers showed longer lifetimes and increased fluorescence.  The dimer design with dyes templated nearest to crossovers had an intense, narrow absorption peak with minimal signs of heterogeneity. Dye attachments in double-tile constructs formed a crossover between two single tiles with strongly coupled homogeneous aggregates.	Crossover junctions are important features on the DNA template. Crossovers may provide ideal environments for dyes and aggregates within the tile, and may at least partially protect or isolate the dyes/aggregates from the local surrounding environment.
3. Dyes templated on complementary strands can drive alternative higher-order constructs during annealing through dye-dye interactions.	Fig. 10 depicts a double-tile model and AFM images. Fig. 12 suggests that dye-dye interactions drive the formation of higher-order constructs. See sections 3.3.1–3.3.3.	Multiple dyes can be strategically templated on complementary strands to promote double-tile formation, or multiple dyes can be templated to a single strand to disentangle dye-dye interactions from construct assembly.
4. Purification by PAGE (or other methods) is often necessary to understand the degree of structural heterogeneity in multi-dye systems.	Fig. 9 and S2–S7† show multiple bands in the PAGE gel that indicate that multiple constructs are present in the sample.	DNA/dye systems with complex dye absorption spectra may contain multiple configurations of DNA that need to be separated by PAGE or other methods for characterization or further use.
5. Multiple characteristic absorption features can indicate heterogeneity and a need for further purification.	Fig. 13 shows multiple traces with distinct absorption features at characteristic dimer and tetramer wavelengths. The heterogeneous nature of the sample, that is, distinct dimer and tetramers were present, was confirmed <i>via</i> TA (section S10†).	The presence of multiple distinct absorption peaks or broad, indistinct absorption features may indicate heterogeneity and a need for purification.
6. Intercalation of a monomer ( <i>e.g.</i> , at a crossover) can suppress isomerization and increase excited-state lifetime.	Table 2; sections 3.1.4 and S4.†	Intercalation of <b>SQ-Cl<sub>2</sub></b> monomers (and likely similar dyes with minimal sterics and rotating single bonds in the conjugated pi-bond network) can be leveraged to increase the lifetime of an excitation and increase the probability of converting excitation energy to fluorescence.
7. <b>SQ-Cl<sub>2</sub></b> (and similar dyes) have characteristic absorption features for H-like aggregates that can inform the number of dyes in an aggregate.	Dimers typically had an absorption peak near 600 nm. See Fig. 6–9 and 13.  Tetramers had a strong narrow absorption peak near 573 nm. See Fig. 9, 11, 13, and 16. Suspected larger aggregates had absorption peaks that were further blue-shifted. See Fig. 9 and S9.†	Spectra can be qualitatively evaluated for the presence of certain aggregates/constructs by observing absorption features. For example, absorption features at higher energy than characteristic dimer absorption maxima can be expected to contain aggregates with more than two dyes.
8. Many designs can form double-tile constructs to some degree, but only certain designs are efficient in terms of yield.	PAGE images in Fig. 9 and S2–S7† show faint low-mobility bands for several designs; however, <b>D17</b> and <b>D18</b> were drastically more efficient in forming double-tile constructs than intermediate designs such as <b>D19</b> (Fig. S5†) or the double-tile-dimer formed by monomer <b>M6</b> (Fig. 9).	Certain locations on the tile are conducive to forming double tiles. We hypothesize that these locations are related to the rotation of the DNA helix and the geometry of the templated bases. Periodic locations ( <i>i.e.</i> , every full turn of the helix) appear favorable for double-tile assembly.
9. Yields of double-tile constructs are improved by optimizing sample conditions, processing, and dye placement.	Absorption spectra in Fig. 13 demonstrates control of sample contents by optimizing sample conditions. Fig. S5† shows a low yield of double tiles when one dye attachment location was altered by a single base.	Double-tile formation can be promoted or suppressed using sample conditions, dye placement, and heat treatments ( <i>e.g.</i> , see Fig. 12–14).



Table 5 (Contd.)

Finding/factor	Evidence	Implications/impacts
10. Dye/DNA concentrations during annealing directly impact construct formation in double-tile constructs.	Fig. 13 shows that higher concentrations of DNA/dyes during annealing lead to more double tiles in the solution. See section 3.3.3.	DNA/dye concentration is a critical variable for designs that can form double-tile constructs.
11. Annealing schedules can be customized to tune sample contents between single-tile and double-tile constructs for certain designs and act as a purification method.	Fig. 14 shows that a strategic annealing schedule promoted formation of double tiles and reduced heterogeneity. See section 3.3.3.	Wavelength-dependent melting profiles ( <i>e.g.</i> , see Fig. 12) can inform the annealing process by identifying temperature treatments that promote or suppress formation of the desired construct through dye–dye interactions. Psudeo-purification by optimized annealing schedules— <i>versus</i> mechanical means—can be preferred due to lower impact on the sample, fewer processing steps, and potentially higher yields.
12. The concentration of $Mg^{2+}$ can be varied (within limits) to promote formation of double-tile constructs.	Fig. 13 shows that high $Mg^{2+}$ resulted in a greater proportion of double tiles <i>versus</i> single tiles for the same annealed concentration. See section 3.3.3.	$Mg^{2+}$ can be varied to gain insight into construct formation; high concentrations can promote aggregation, but in excess can lead to unwanted “runaway” aggregation resulting in large clusters of dyes/DNA ( <i>e.g.</i> , see section S2 and Fig. S8†).
13. Double tiles—once formed during annealing—are robust to changes in DNA concentration.	Fig. 13 shows that double-tile spectra are maintained after dilution.	Double tiles—once formed during annealing—can be transferred to environments that are <i>not</i> favorable for their initial assembly without dissociating into single tiles.
14. Multiple <b>SQ-Cl<sub>2</sub></b> dyes templated in a cluster on a single tile appear to distort the tile, resulting in multiple higher-order constructs or causing the dyes and DNA to aggregate into large masses of material.	Fig. 9 shows only faint bands that had high-mobility (single-tiles) for designs with more than two dyes templated to a single tile ( <i>i.e.</i> , <b>Tri1</b> and <b>Tet1</b> ), with a significant amount of material appearing in lower-mobility bands representing either mis-folded or uncontrolled aggregation of tiles (see also Fig. S8†).	Limits may exist to the number of (hydrophobic) dyes per quantity of DNA that can be reliably arranged to form aggregates. We suggest that excess dyes imparted additional dye–dye interactions and hydrophobicity on the system that can impede formation of the desired constructs.
15. Aggregate coupling and exciton delocalization can be maintained after transfer to solid phase.	Fig. 16 shows that aggregate absorption spectra are largely unchanged in solid phase—apart from a consistent solvent-related red-shift—compared to solution-phase samples. See section 3.3.5.	Constructs can be prepared in solution under conditions optimal for an individual sample, then transferred to solid phase while maintaining desired properties.

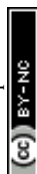
Furthermore, we showed that the inter-dye attractive forces can be harnessed as part of the self-assembly process to direct and optimize the assembly of larger DNA-aggregate systems. In the double-tile constructs developed here, a combination of dye–dye interactions along with sample design, sample conditions, and annealing treatment worked cooperatively to drive the system to form a double-tile arrangement. The double-tile structures were characterized by a strongly coupled homogeneous tetramer attached to bases at the site of a newly formed crossover that combined what might be viewed at first glance to be two distinct DX tiles (Fig. 10). Importantly, however, these double tiles formed during the annealing process around a self-optimized tetramer rather than combining two independent single tiles through a branch-migration process. Furthermore, our results suggested that the formation of the additional crossover joining the two tiles was a general phenomenon in that similar aggregate-driven crossovers between distinct constructs could be formed at appropriate, periodic, locations based on the rotation of the helix along the helical axis.

The double-tile system provided tunability in multiple aspects. The constructs were structurally and spectrally tunable through changing sample conditions (*e.g.*, concentration, buffer conditions), dye placement, and heat treatments

to promote single-tile dimers or double-tile tetramers, which provided a means of selecting between  $\sim 600$  nm and  $\sim 570$  nm absorption maxima. The DX tile format thus provides additional pathways for adjusting and optimizing the formation of double-tile constructs through careful design of component strands and dye attachments to direct the assembly order of constructs during annealing.

Importantly, our results demonstrated that the properties of select constructs—including **M8**, **D7**, **D17**, and **D18**—were robust after the samples were annealed. That is, after annealing, the optical properties were largely insensitive to changes in DNA concentration and buffer conditions. In the case of **M8**, the optical response was practically unchanged from standard solution conditions ( $1\times$  TBE, 15 mM  $MgCl_2$ ) to solid (dry) phase (Fig. 5d). Dimer **D7** exhibited a small red-shift when dried, but otherwise maintained its characteristic dimer spectra (Fig. 16b). The dry **D7** absorption spectrum demonstrated—to our knowledge—the first observation of exciton delocalization in a DNA-templated dye-aggregate in solid phase.

The double-tile constructs were similarly robust. Fig. 13a and b show that the absorption spectrum of **DT1** was largely unchanged over roughly two orders of magnitude of DNA concentration. Additionally, the absorption spectra—and by exten-



sion, the exciton delocalization—were maintained between standard (15 mM) and high (100 mM)  $\text{Mg}^{2+}$  concentrations. Furthermore, the absorption and CD spectra were largely maintained when transferred to solid phase, implying that the aggregates were robust at extreme  $\text{Mg}^{2+}$  and DNA concentrations as the solvent evaporated and the samples adsorbed onto the slide. Similar to **D7**, the spectra for the dried double-tile samples reflected their solution-phase counterparts. We note that the liquid-phase double-tile absorption spectra were robust when subjected to elevated temperatures (but below the DNA melting temperature) up to 50 °C (ESI section S7†). Additionally, the solid-phase double-tile sample absorption spectra were robust when heated to 80 °C, well above the DNA melting temperature (ESI section S7†). We also note that the strong CD signal from the double-tile aggregates enabled observation of CD from the solid-phase samples that contained otherwise achiral dyes, again confirming that exciton delocalization was maintained in solid phase for the four-dye aggregates.

The robust nature of the templated aggregates is of both fundamental and technological importance. Our results suggest that the single and double tiles in this study are suitable building blocks for in-solution assembly of complex DNA-dye networks composed of multiple distinct DX tile modules that can be subsequently immobilized on a surface while maintaining their optical properties. Although we did not emphasize TA experiments in our study, we also note that the extended ( $\sim 2\times$ ) lifetimes observed in the double-tile tetramers relative to the **D7** dimer are of particular interest. Advanced applications involving exciton exchange will require that excited-state lifetimes are long enough to enable exciton transfer before the system relaxes to the ground state. Further investigation of the excited-state dynamics of these aggregates are warranted but were beyond the scope of the current work.

Throughout this paper we have identified the importance of factors, such as dye attachment positions, sample conditions (including concentration and salt conditions), and annealing schedule—as well as other specific findings—that influence the final configuration and properties of the DX-tile DNA-dye system. Often, these findings and factors have been underappreciated in the roles that they play in determining final outcomes. Table 5 highlights these factors, their supporting evidence, and potential implications for developing design rules to create and arrange dyes and aggregates with desirable properties. These 15 relevant findings and factors could be relevant for other similar system-level investigations.

The finding and factors in Table 5 are ordered in rough correspondence to the overall flow of their occurrence in the main text: for example, starting with dye attachment location considerations before progressing to specific elements of sample conditions and starting with monomer considerations before progressing to findings and factors associated with multiple dye aggregates and the more complex effects on DNA configurations. Conversely, to address different reader interests, Table 6 below identifies for each potential topical area of interest the corresponding Table 5 findings and factors.

**Table 6** Summary of findings and factors from Table 5 by topic

Topic	Relevant finding/factor no.
Role of dye number and attachment location(s)	1–3, 7, & 14
Role of sample conditions	9, 10, 12, & 13
Role of annealing conditions and schedules	10 & 11
Monomer properties	1, 2, & 6
Multiple-dye aggregate properties	1–3, 7, 12, & 14
Double-tile assembly	2, 3, 8–13, & 15
Reducing heterogeneity	4, 5, & 11
Transferring to solid phase	15

## 5. Conclusions

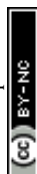
In this study, we have demonstrated examples of one-, two-, and four-dye prototype constructs based on the DX-DAE DNA tile templated with single-linked hydrophobic squaraine dyes. In addition to optimized monomer and dimer constructs, we demonstrated a DNA-dye system that utilizes both DNA and dye interactions in a cooperative manner to arrive at final constructs with desirable optical properties. This view represents an important paradigm shift in the design space for templating dye aggregates with DNA in that one must not only account for dye-dye interactions, but one can also leverage those interactions to drive construct assembly. That is, the dye interactions themselves may contribute to (and even help direct) the final DNA configuration. Furthermore, the robust nature of the final constructs suggests that distinct tile building blocks can be formed under optimal conditions and then transferred to other buffer environments for higher order assembly while maintaining their spectral properties. These findings are important for developing an understanding of DNA-dye systems to apply in further developing modular and complex systems (*e.g.*, *via* sticky-end assembly) for advanced applications.

## Author contributions

WBK, BY, JL, SKR, and JAH contributed to the original conceptualization and design of the study. OAM, KC-S, RDP, and BY participated in additional conversations and experimental design. RDP performed TA experiments and GTA. NO and PHD performed AFM image acquisition, image processing, and data analysis and assisted in AFM protocol development, data interpretation, and development of Fig. 10c. SKR prepared all samples and conducted all other sample characterizations and analyses, including KRM modeling. SKR and JAH contributed to writing the original draft. All authors contributed to review and editing.

## Data availability

ESI including DNA sequences, PAGE gel images, fluorescence data processing details, additional absorption and fluo-



rescence data, KRM modeling details, AFM details and protocol, melting profiles, transient absorption and associated GTA, and images of solid phase sample are available in the ESI.† Underlying data for the study will be available through (ScholarWorks, Boise State University Albertsons Library, etc.) within 90 days of publication.

## Conflicts of interest

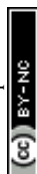
The authors have no conflicts of interest to declare.

## Acknowledgements

Research at Boise State University, including data collection, analysis, interpretation, manuscript preparation, and specific equipment purchases including the CD spectrometer was supported by the U.S. Department of Energy (DOE), Office of Basic Energy Sciences, Division of Materials Science and Engineering through the Established Program to Stimulate Competitive Research (EPSCoR), under Award No. DE-SC0020089. Specific equipment, including the femtosecond transient absorption, TCSPC, and UV-Vis spectrometers, was supported by the Department of the Navy, Office of Naval Research (ONR), under ONR Award No. N00014-19-1-2615. The Bruker Dimension FastScan Bio AFM used in this work is located in the Boise State University Surface Science Laboratory (SSL), which is part of the FaCT Core Facility, RRID: SCR-024733, that receives support from the National Institutes of Health under the Institutional Development Awards Program of the National Institute of General Medical Sciences via grants no. P20GM148321 and P20GM103408, the former of which also partially supports co-author PHD. The authors thank Dr C. M. Efav for assistance with AFM imaging, Dr S. Basu for providing experimental data on SQ-Cl<sub>2</sub> free dyes, and Dr A. Biaggne for help with DNA visualization.

## References

- 1 D. Mathur, S. A. Díaz, N. Hildebrandt, R. D. Pensack, B. Yurke, A. Biaggne, L. Li, J. S. Melinger, M. G. Ancona, W. B. Knowlton and I. L. Medintz, *Chem. Soc. Rev.*, 2023, **52**, 7848–7948.
- 2 H. Bui, S. A. Díaz, J. Fontana, M. Chiriboga, R. Veneziano and I. L. Medintz, *Adv. Opt. Mater.*, 2019, **7**, 1900562.
- 3 S. M. Hart, J. Gorman, M. Bathe and G. S. Schlau-Cohen, *Acc. Chem. Res.*, 2023, **56**, 2051–2061.
- 4 E. E. Jelley, *Nature*, 1936, **138**, 1009–1010.
- 5 G. Scheibe, *Kolloid-Z.*, 1938, **82**, 1–14.
- 6 M. Kasha, H. R. Rawls and M. A. El-Bayoumi, *Pure Appl. Chem.*, 1965, **11**, 371–392.
- 7 M. Kasha, *Radiat. Res.*, 1963, **20**, 55.
- 8 F. Fassioli, R. Dinshaw, P. C. Arpin and G. D. Scholes, *J. R. Soc. Interface*, 2014, **11**, DOI: [10.1098/rsif.2013.0901](https://doi.org/10.1098/rsif.2013.0901).
- 9 D. Abramavicius and S. Mukamel, *J. Phys. Chem. B*, 2009, **113**, 6097–6108.
- 10 T. Mirkovic, E. E. Ostroumov, J. M. Anna, R. Van Grondelle, Govindjee and G. D. Scholes, *Chem. Rev.*, 2017, **117**, 249–293.
- 11 G. D. Scholes and C. Smyth, *J. Chem. Phys.*, 2014, **140**, 110901.
- 12 *Visions of DNA Nanotechnology at 40 for the Next 40*, ed. N. Jonoska and E. Winfree, Springer Nature, Singapore, 2023.
- 13 T. Wang, T. Bai, Z. Tan, Y. P. Ohayon, R. Sha, S. Vecchioni, N. C. Seeman and B. Wei, *J. Am. Chem. Soc.*, 2023, **145**, 2455–2460.
- 14 S. Vecchioni, R. Lo, Q. Huang, K. Wang, Y. P. Ohayon, R. Sha, L. J. Rothschild and S. J. Wind, *Small*, 2024, **2407604**, 1–11.
- 15 C. Zhang, M. Zheng, Y. P. Ohayon, S. Vecchioni, R. Sha, N. C. Seeman, N. Jonoska and C. Mao, *J. Am. Chem. Soc.*, 2022, **144**, 8741–8745.
- 16 W. Wang, C. Chen, S. Vecchioni, T. Zhang, C. Wu, Y. P. Ohayon, R. Sha, N. C. Seeman and B. Wei, *Angew. Chem., Int. Ed.*, 2021, **60**, 25781–25786.
- 17 X. Zhou, D. Satyabola, H. Liu, S. Jiang, X. Qi, L. Yu, S. Lin, Y. Liu, N. W. Woodbury and H. Yan, *Angew. Chem., Int. Ed.*, 2022, **61**, e202211200.
- 18 K. Szaciłowski, *Chem. Rev.*, 2008, **108**, 3481–3548.
- 19 W. Wu and G. D. Scholes, *J. Phys. Chem. Lett.*, 2024, **15**, 4056–4069.
- 20 M. A. Castellanos, A. Dodin and A. P. Willard, *Phys. Chem. Chem. Phys.*, 2020, **22**, 3048–3057.
- 21 B. Yurke, R. Elliott and A. Sup, *Phys. Rev. A*, 2023, **107**, 12603.
- 22 B. Yurke, in *Visions of DNA Nanotechnology at 40 for the next 40*, ed. N. Jonoska and E. Winfree, Springer Nature, Singapore, 2023, vol. Part F821, pp. 125–169.
- 23 S. Jiang, H. Yan and Y. Liu, *ACS Nano*, 2014, **8**, 5826–5832.
- 24 N. R. Kallenbach, R. I. Ma and N. C. Seeman, *Nature*, 1983, **305**, 829–831.
- 25 E. Winfree, F. Liu, L. A. Wenzler and N. C. Seeman, *Nature*, 1998, **394**, 539–544.
- 26 F. Tsu-Ju and N. C. Seeman, *Biochemistry*, 1993, **32**, 3211–3220.
- 27 X. Li, X. Yang, J. Qi and N. C. Seeman, *J. Am. Chem. Soc.*, 1996, **118**, 6131–6140.
- 28 K. L. Lau and H. F. Sleiman, *ACS Nano*, 2016, **10**, 6542–6551.
- 29 M. Wang, H. Huang, Z. Zhang, S. J. Xiao, S.-J. Xiao and S. J. Xiao, *Nanoscale*, 2016, **8**, 18870–18875.
- 30 W. Zhang, C. Jiang, X. Guo, M. Muhammad Faran Ashraf Baig, C. Ni and S. J. Xiao, *J. Colloid Interface Sci.*, 2022, **616**, 499–508.
- 31 C. Jiang, B. Lu, W. Zhang, Y. P. Ohayon, F. Feng, S. Li, N. C. Seeman and S. J. Xiao, *J. Am. Chem. Soc.*, 2022, **144**, 6759–6769.
- 32 J. Son, J. Lee, A. Tandon, B. Kim, S. Yoo, C. W. Lee and S. H. Park, *Nanoscale*, 2015, **7**, 6492–6497.



- 33 B. L. Cannon, L. K. Patten, D. L. Kellis, P. H. Davis, J. Lee, E. Graugnard, B. Yurke and W. B. Knowlton, *J. Phys. Chem. A*, 2018, **122**, 2086–2095.
- 34 J. S. Huff, D. B. Turner, O. A. Mass, L. K. Patten, C. K. Wilson, S. K. Roy, M. S. Barclay, B. Yurke, W. B. Knowlton, P. H. Davis and R. D. Pensack, *J. Phys. Chem. B*, 2021, **125**, 10240–10259.
- 35 J. S. Huff, P. H. Davis, A. Christy, D. L. Kellis, N. Kandadai, Z. S. D. Toa, G. D. Scholes, B. Yurke, W. B. Knowlton and R. D. Pensack, *J. Phys. Chem. Lett.*, 2019, **10**, 2386–2392.
- 36 J. S. Huff, S. A. Díaz, M. S. Barclay, A. U. Chowdhury, M. Chiriboga, G. A. Ellis, D. Mathur, L. K. Patten, S. K. Roy, A. Sup, A. Biaggne, B. S. Rolczynski, P. D. Cunningham, L. Li, J. Lee, P. H. Davis, B. Yurke, W. B. Knowlton, I. L. Medintz, D. B. Turner, J. S. Melinger and R. D. Pensack, *J. Phys. Chem. C*, 2022, **126**, 17164–17175.
- 37 S. A. Díaz, G. Pascual, L. K. Patten, S. K. Roy, A. Meares, M. Chiriboga, K. Susumu, W. B. Knowlton, P. D. Cunningham, D. Mathur, B. Yurke, I. L. Medintz, J. Lee and J. S. Melinger, *Nanoscale*, 2023, **15**, 3284–3299.
- 38 M. S. Barclay, C. K. Wilson, S. K. Roy, O. A. Mass, O. M. Obukhova, R. P. Svoiakov, A. L. Tatarets, A. U. Chowdhury, J. S. Huff, D. B. Turner, P. H. Davis, E. A. Terpetschnig, B. Yurke, W. B. Knowlton, J. Lee and R. D. Pensack, *ChemPhotoChem*, 2022, **6**, e202200039.
- 39 M. S. Barclay, S. K. Roy, J. S. Huff, O. A. Mass, D. B. Turner, C. K. Wilson, D. L. Kellis, E. A. Terpetschnig, J. Lee, P. H. Davis, B. Yurke, W. B. Knowlton and R. D. Pensack, *Commun. Chem.*, 2021, **4**, 19.
- 40 N. D. Wright, J. S. Huff, M. S. Barclay, C. K. Wilson, G. Barcenás, K. M. Duncan, M. Ketteridge, O. M. Obukhova, A. I. Krivoshey, A. L. Tatarets, E. A. Terpetschnig, J. C. Dean, W. B. Knowlton, B. Yurke, L. Li, O. A. Mass, P. H. Davis, J. Lee, D. B. Turner and R. D. Pensack, *J. Phys. Chem. A*, 2023, **127**, 1141–1157.
- 41 O. A. Mass, C. K. Wilson, S. K. Roy, M. S. Barclay, L. K. Patten, E. A. Terpetschnig, J. Lee, R. D. Pensack, B. Yurke and W. B. Knowlton, *J. Phys. Chem. B*, 2020, **124**, 9636–9647.
- 42 O. A. Mass, C. K. Wilson, G. Barcenás, E. A. Terpetschnig, O. M. Obukhova, O. S. Kolosova, A. L. Tatarets, L. Li, B. Yurke, W. B. Knowlton, R. D. Pensack and J. Lee, *J. Phys. Chem. C*, 2022, **126**, 3475–3488.
- 43 S. Basu, S. K. Roy, G. Barcenás, L. Li, B. Yurke, W. B. Knowlton and J. Lee, *Biochemistry*, 2023, **62**, 3234–3244.
- 44 K. M. Duncan, H. M. Byers, M. E. Houdek, S. K. Roy, A. Biaggne, M. S. Barclay, L. K. Patten, J. S. Huff, D. L. Kellis, C. K. Wilson, J. Lee, P. H. Davis, O. A. Mass, L. Li, D. B. Turner, J. A. Hall, W. B. Knowlton, B. Yurke and R. D. Pensack, *J. Phys. Chem. A*, 2023, **127**, 4901–4918.
- 45 P. Sa-Ardyen, A. V. Vologodskii and N. C. Seeman, *Biophys. J.*, 2003, **84**, 3829–3837.
- 46 P. H. Von Hippel, N. P. Johnson and A. H. Marcus, *Biopolymers*, 2013, **99**, 923–954.
- 47 K. Cervantes-Salguero, M. Kadrmas, B. M. Ward, D. Lysne, A. Wolf, L. Piantanida, G. Pascual and W. B. Knowlton, *Langmuir*, 2024, **40**, 10195–10207.
- 48 J. Y. Lee, Q. Yang, X. Chang, M. Jeziorek, D. Perumal, T. R. Olivera, J. P. Etchegaray and F. Zhang, *Nanoscale*, 2024, **16**, 1685–1691.
- 49 M. Chiriboga, S. A. Díaz, D. Mathur, D. A. Hastman, J. S. Melinger, R. Veneziano and I. L. Medintz, *J. Phys. Chem. B*, 2022, **126**, 110–122.
- 50 E. Boulais, N. P. D. Sawaya, R. Veneziano, A. Andreoni, J. L. Banal, T. Kondo, S. Mandal, S. Lin, G. S. Schlau-Cohen, N. W. Woodbury, H. Yan, A. Aspuru-Guzik and M. Bathe, *Nat. Mater.*, 2018, **17**, 159–166.
- 51 J. L. Banal, T. Kondo, R. Veneziano, M. Bathe and G. S. Schlau-Cohen, *J. Phys. Chem. Lett.*, 2017, **8**, 5827–5833.
- 52 S. M. Hart, W. J. Chen, J. L. Banal, W. P. Bricker, A. Dodin, L. Markova, Y. Vyborna, A. P. Willard, R. Häner, M. Bathe and G. S. Schlau-Cohen, *Chem*, 2021, **7**, 752–773.
- 53 S. M. Hart, X. Wang, J. Guo, M. Bathe and G. S. Schlau-Cohen, *J. Phys. Chem. Lett.*, 2022, 1863–1871.
- 54 P. D. Cunningham, W. P. Bricker, S. A. Díaz, I. L. Medintz, M. Bathe and J. S. Melinger, *J. Chem. Phys.*, 2017, **147**, 055101.
- 55 O. A. Mass, D. R. Watt, L. K. Patten, R. D. Pensack, J. Lee, D. B. Turner, B. Yurke and W. B. Knowlton, *Phys. Chem. Chem. Phys.*, 2023, **25**, 28437–28451.
- 56 K. M. Duncan, D. L. Kellis, J. S. Huff, M. S. Barclay, J. Lee, D. B. Turner, P. H. Davis, B. Yurke, W. B. Knowlton and R. D. Pensack, *Molecules*, 2022, **27**, 6612.
- 57 P. D. Cunningham, Y. C. Kim, S. A. Díaz, S. Buckhout-White, D. Mathur, I. L. Medintz and J. S. Melinger, *J. Phys. Chem. B*, 2018, **122**, 5020–5029.
- 58 S. K. Roy, O. A. Mass, D. L. Kellis, C. K. Wilson, J. A. Hall, B. Yurke and W. B. Knowlton, *J. Phys. Chem. B*, 2021, **125**, 13670–13684.
- 59 B. A. Armitage, *Top. Curr. Chem.*, 2005, **253**, 55–76.
- 60 G. Pascual, S. K. Roy, G. Barcenás, C. K. Wilson, K. Cervantes-Salguero, O. M. Obukhova, A. I. Krivoshey, E. A. Terpetschnig, A. L. Tatarets, L. Li, B. Yurke, W. B. Knowlton, O. A. Mass, R. D. Pensack and J. Lee, *Nanoscale*, 2023, **16**, 1206–1222.
- 61 E. Freytag, L. Kreimendahl, M. Holzapfel, J. Petersen, H. Lackinger, M. Stolte, F. Würthner, R. Mitric and C. Lambert, *J. Org. Chem.*, 2023, **88**, 10777–10788.
- 62 S. M. Hart, J. L. Banal, M. A. Castellanos, L. Markova, Y. Vyborna, J. Gorman, R. Häner, A. P. Willard, M. Bathe and G. S. Schlau-Cohen, *Chem. Sci.*, 2022, **13**, 13020–13031.
- 63 O. A. Mass, S. Basu, L. K. Patten, E. A. Terpetschnig, A. I. Krivoshey, A. L. Tatarets, R. D. Pensack, B. Yurke, W. B. Knowlton and J. Lee, *J. Phys. Chem. Lett.*, 2022, **13**, 10688–10696.
- 64 G. Barcenás, A. Biaggne, O. A. Mass, C. K. Wilson, O. M. Obukhova, O. S. Kolosova, A. L. Tatarets, E. Terpetschnig, R. D. Pensack, J. Lee, W. B. Knowlton, B. Yurke and L. Li, *RSC Adv.*, 2021, **11**, 19029–19040.



- 65 D. L. Kellis, C. Sarter, B. L. Cannon, P. H. Davis, E. Graugnard, J. Lee, R. D. Pensack, T. Kolmar, A. Jäschke, B. Yurke and W. B. Knowlton, *ACS Nano*, 2019, **13**, 2986–2994.
- 66 O. Kühn, T. Renger and V. May, *Chem. Phys.*, 1996, **204**, 99–114.
- 67 O. A. Mass, C. K. Wilson, S. K. Roy, M. S. Barclay, L. K. Patten, E. A. Terpetschnig, J. Lee, R. D. Pensack, B. Yurke and W. B. Knowlton, *J. Phys. Chem. B*, 2020, **124**, 9636–9647.
- 68 V. Czikkely, H. D. Forsterling and H. Kuhn, *Chem. Phys. Lett.*, 1970, **6**, 207–210.
- 69 T. Holstein, *Ann. Phys.*, 1959, **8**, 325–342.
- 70 J. Frenkel, *Phys. Rev.*, 1931, **37**, 1276–1294.
- 71 P. R. Heenan and T. T. Perkins, *ACS Nano*, 2019, **13**, 4220–4229.
- 72 K. Huang and A. Rhys, *Proc. R. Soc. London, Ser. A*, 1950, **204**, 406–423.
- 73 L. Lerman, *J. Mol. Biol.*, 1961, **3**, 18–30.
- 74 S. M. Yarmoluk, S. S. Lukashov, T. Y. Ogul'Chansky, M. Y. Losytsky and O. S. Korniyushyna, *Biopolymers*, 2001, **62**, 219–227.
- 75 H. Asanuma, T. Fujii, T. Kato and H. Kashida, *J. Photochem. Photobiol., C*, 2012, **13**, 124–135.
- 76 A. Köhler and H. Bässler, *Electronic Processes in Organic Semiconductors: An Introduction*, Wiley-VCH Verlag GmbH & Co. KGaA, Weinheim, Germany, 1st edn, 2015.
- 77 F. Momicchioli, A. S. Tatikolov, D. Vanossi and G. Ponterini, *Photochem. Photobiol. Sci.*, 2004, **3**, 396–402.
- 78 D. Sarkar, P. Das, S. Basak and N. Chattopadhyay, *J. Phys. Chem. B*, 2008, **112**, 9243–9249.
- 79 A. Sanchez-Galvez, P. Hunt, M. A. Robb, M. Olivucci, T. Vreven and H. B. Schlegel, *J. Am. Chem. Soc.*, 2000, **122**, 2911–2924.
- 80 A. S. Tatikolov and S. M. B. Costa, *J. Photochem. Photobiol., A*, 2001, **140**, 147–156.
- 81 J. S. Huff, D. B. Turner, O. A. Mass, L. K. Patten, C. K. Wilson, S. K. Roy, M. S. Barclay, B. Yurke, W. B. Knowlton, P. H. Davis and R. D. Pensack, *J. Phys. Chem. B*, 2021, **125**, 10240–10259.
- 82 M. Kasha, *Discuss. Faraday Soc.*, 1950, **9**, 14–19.
- 83 C. Zheng, C. Zhong, C. J. Collison and F. C. Spano, *J. Phys. Chem. C*, 2019, **123**, 3203–3215.
- 84 N. J. Hestand and F. C. Spano, *Chem. Rev.*, 2018, **118**, 7069–7163.
- 85 K. Cervantes-Salguero, A. Biaggne, J. M. Youngsman, B. M. Ward, Y. C. Kim, L. Li, J. A. Hall, W. B. Knowlton, E. Graugnard and W. Kuang, *Int. J. Mol. Sci.*, 2022, **23**, 1–18.
- 86 H. Kashida, T. Fujii and H. Asanuma, *Org. Biomol. Chem.*, 2008, **6**, 2892–2899.
- 87 B. L. Cannon, D. L. Kellis, L. K. Patten, P. H. Davis, J. Lee, E. Graugnard, B. Yurke and W. B. Knowlton, *J. Phys. Chem. A*, 2017, **121**, 6905–6916.

